INVESTIGATING THE ELECTRONIC AND STRUCTURAL PROPERTIES OF STANENE

A THESIS

SUBMITTED TO THE GRADUATE SCHOOL

IN PARTIAL FULFILLMENT OF THE REQUIREMENTS

FOR THE DEGREE

MASTER OF SCIENCE

BY

KAELYN FERRIS

ADVISOR: DR. ANTONIO CANCIO

BALL STATE UNIVERSITY

MUNCIE, INDIANA

MAY 2018

Contents

List of Figures

List of Tables

Abstract

This study investigates the structural and electronic properties of two-dimensional tin, known as stanene, under compressive biaxial strain using Density Functional Theory (DFT). Stanene possesses a buckled honeycomb-like structure and is a potential candidate for a quantum spin Hall (QSH) insulator in which a quantum Hall effect is generated in the absence of a magnetic field due to strong spin-orbit coupling (SOC). This effect, in combination with a strain-tunable band gap, makes stanene an interesting material for spintronic applications. Stanene is stable in both a high-buckled (HB) configuration, which is metallic, and a low-buckled (LB) configuration, which gives rise to a QSH insulating phase, and a transition between the two can be induced through strain. For a monolayer of tin, the HB phase is more stable. This study then investigates whether multiple layers of tin can ensure the LB phase remains the most stable configuration. This work is acheived using the plane-wave pseudopotential code, ABINIT, which can accurately reproduce all-electron calculations of ground-state energies and densitities which are then used to determine the ground state structural and electronic properties. A Becke-Johnson correction to band structure calculations is also introduced in order improve the band structure eigenvalues of the LB phase of stanene.

Acknowledgements

First and perhaps most importantly, I need to thank Dr. Cancio for his seemingly endless well of patience and tactful advice. It has been a long journey of collecting achievements and it finally appears that I have completed this final level. Without his guidance and helpful explanation, I would perhaps still be running through the dark, unequipped to think scientifically, as he has made me. For that, I would like to give him my sincerest thanks.

Additionally, I would like to thank my committee. I recognize the time and effort required of its members and I appreciate you doing so. In particular, I would like to thank Dr. Khatun, not only for her membership on this committee, but also for the productive discussions she has provided during our CCN meetings.

Finally, I would like to thank my fellow graduate student colleagues, Dylan Griffith, Samuel Teye, Lillie Robinson, and Albert DiBenedetto. Their compansionship and help through the countless difficult problem sets and coursework over these last two years has helped build the confidence needed for my academic success. Chiefly, I would like to thank Albert for his camaraderie while we both underwent the marathon that is writing a thesis.

Chapter 1

Introduction

Two-dimensional materials, also known as monolayer materials, have recently garnered significant interest within the field of condensed matter physics both for the novel physics that have emerged within the study of topology as well as their unique device applications. Within this field are several families of two-dimensional materials, each with their own unique structural and electronic properties, which include: transition-metal dichalcogenides (TMDs), graphene and its analogues made from the Group IV elements of the periodic table (such as silicene), phosphorene-like materials, and the Group III-VI family of semiconductors such as InSe and GaS [8]. Many of these materials have enormous potential for fabricating high-efficiency field effect transistors [9], photovoltaics [10], and energy storage [11]. Of specific interest to this thesis is the emergence of the quantum Hall and quantum-spin Hall effect that is present in some of these materials. This has brought the interest of spintronic device applications forward, of which graphene and the other Group IV monolayers prove to be some of the most promising candidates.

1.1 Graphene and the Graphene Family

Graphene is one of the most thoroughly studied two-dimensional materials primarily because of its enormous range of electronic device applications, high-carrier mobility, and

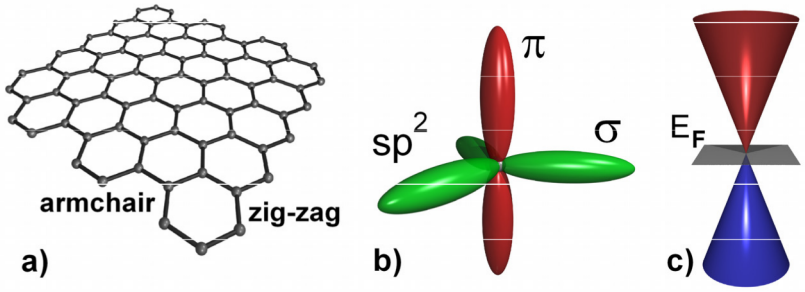

Figure 1.1: (a) Structure of graphene depicting the two edge types, armchair and zig-zag, (b) depiction of sp^2 hybridized bonds (green) and the delocalized π bond (red) in graphene, and (c) schematic of a dirac cone found at the K point in graphene. Image taken from [1].

exotic physics that have emerged from it [1]. The structure of graphene is that of a two-dimensional sheet of carbon atoms arranged in a honeycomb structure (Figure 1.1). Its unique structural properties include a large breaking strength of 42 N/m and a Young's modulus (the ratio of stress to strain of a material) of $\approx$ 1.0 TPa, making defect free graphene one of the strongest materials ever measured [12]. In addition, graphene also has an extremely high room temperature thermal conductivity of $\approx 5 \times 10^3$ W/mK [13] and a monolayer membrane is impermeable to gases, including helium [14].

Carbon has four valence electrons, and in graphene three of these electrons bond in-plane in an sp^2 hybridized configuration while the fourth valence electron occupies an orbital perpendicular to the monolayer in a delocalized π-bond, shown in Figure 1.1. This dangling bond enables the monolayer to have high charge carrier mobility and allows for the creation of a two-dimensional electron gas [1]. The high carrier mobility is the result of a linear crossing of valence and conduction bands at the K point (a point of high symmetry in momentum space) creating what are known as Dirac cones. This phenomenon is evidence of charge carriers which behave as though they were massless Dirac fermions. These quasiparticles mimic the physics of typical photons that, instead of moving at the speed of light, move with a speed v_F, known as the fermi velocity, about 300 times smaller than the speed of light, c [15] and give rise to some particularly interesting physics.

Graphene's unique electronic properties also allow for the possibility of interesting

new devices including: field-effect and radio frequency transistors [16], infrared detectors [17], and several unconventional electronic switches ([18], [19], [20], [21]). Most interestingly are its potential applications in spintronics [22] and the emergence of a new category of "Fermi-Dirac" physics due to its linear dispersion of the band structure near the K point. However, the primary difficulty in producing these devices is graphene's lack of a band gap. Solutions have been posed which induce one through a variety of doping and other symmetry breaking mechanisms. One solution to this problem that has been brought forward is to use other Group IV elements to make a monolayer with instead of carbon. These graphene analogs are known as silicene (the monolayer form of $_{14}$Si), germanene (the monolayer form of $_{32}$Ge) and, of particular interest to this thesis, stanene (the monolayer form of $_{50}$Sn). The structure of these materials is very similar to that of graphene, a honeycomb lattice but with basis atoms that are buckled slightly out of plane with each other. This buckling also increases with increasing atomic number as one moves down the Group IV column. These materials still possess the Dirac cone state, but with small band gaps.

One of the consequences of moving down the Group IV column monolayer materials is the increase in atomic mass where relativistic effects such as spin-orbit coupling (SOC) begin to become significant. This spin-orbit interaction induces a band gap at the K point in silicene [23], germanene [24], and stanene [25] which increases with increasing atomic mass. This phenomenon is indicative of what is known as a quantum-spin Hall insulator, described in more detail in Section 2.4.

1.2 A Brief Introduction to Stanene

Stanene is an atomically thin sheet of tin atoms which are arranged in a buckled honeycomb lattice (shown in Figure 1.2). It has been proposed as a quantum-spin Hall insulator and has been experimentally fabricated via molecular beam epitaxy (a common method of thin-film deposition) to a Bi_2Te_3 substrate [2] and using femto-second laser pulses on a target

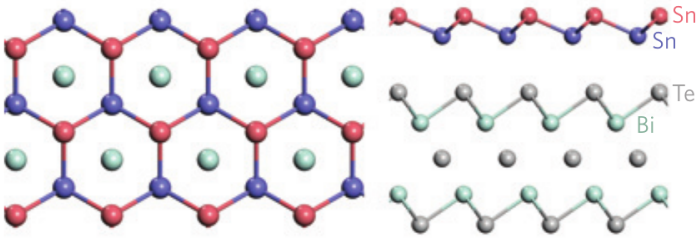

Figure 1.2: Top view (left) and side view(right) of stanene on top of a substrate of Bi_2Te_3 [2].

in a liquid medium [26]. Free standing stanene has a chemically active surface due to the unsaturated pz orbital (an orbital which freely dangles, not bonded to anything) and so its electronic properties are easily affected by substrates [27]. The disipationless edge currents created through the quantum-spin Hall effect, in addition to the spin-orbit induced band gap, make stanene an interesting candidate for spintronic devices and a promising one for a topological insulator (TI)-based field effect transistor [28].

Freestanding stanene is stable in both a high-buckled (HB) and low-buckled (LB) configuration, shown in Figure 1.3. The low-buckled configuration is a TI, exhibiting a quantum-spin Hall insulating phase. The high-buckled phase, however, is metallic and more stable [29]. This appears as an apparent contradiction as the HB and LB phases of stanene are derived from tin's bulk allotropes, β-Sn and α-Sn respectively, of which α-Sn is globally stable at low temperatures. Previous investigations have explored the introduction of a second layer of tin to stabilize the lattice while still preserving its topological properties using density functional theory (DFT) [30]. However, the geometry of this bilayer system was a simple van der Waals stacking which failed to take into account the geometry these layers are derived from. Therefore, an investigation of the structural and electronic properties of realistic freestanding stanene layers remains an unexplored method of stabilization.

1.3 This Work

This thesis will use density functional theory (DFT) to address three basic goals: (1) to confirm that monolayer stanene is a quantum-spin Hall insulator, (2) to introduce multiple

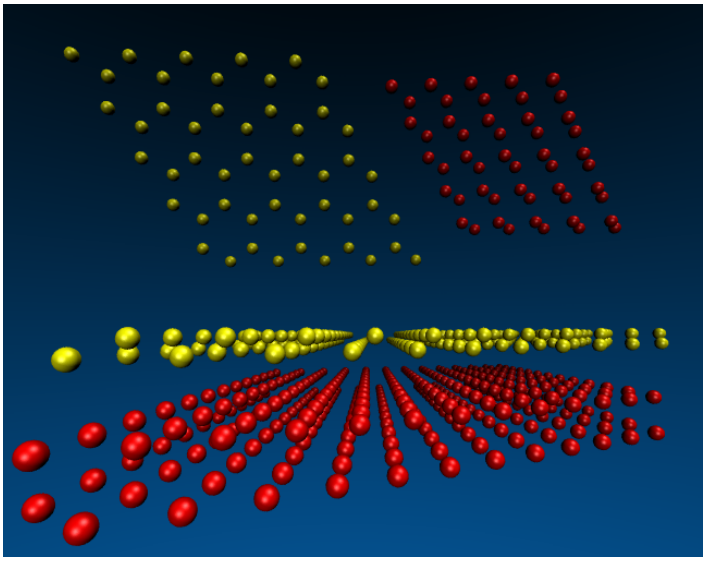

Figure 1.3: Visualization of high-buckled (red) and low-buckled (yellow) stanene from top and side view.

layers in a more realistic geometry as a potential method of stabilization, and (3) utilize the Becke-Johnson method (described at the end of Section 2.2.4), which has been shown to improve eigenvalue calculations in a DFT environment, in order to provide more accurate band structures for monolayer and multilayer stanene.

To accomplish this, Chapter 2 will present a background theory on solids, specifically spin-orbit coupling, the DFT method and how it is implemented, and the family of Hall effects. Chapter 3 discusses the construction of a useful DFT model including: pseudopotential generation, spin-orbit coupling consideration, tests of the Becke-Johnson method, and comparing this model to experiment. Chapter 4 presents the structural and electronic properties of stanene, finding the lattice constant and atom positions within the unit cell, along with a discussion of the band structure and density of states. Chapter 5 explores the structural stability of monolayer, bilayer, and trilayer stanene via compressive biaxial strain followed by a discussion of the electronic structure of multilayer stanene. Finally, chapter 6 summarizes the conclusions of this study and ends with a discussion of future work that can be done.

Chapter 2

Background Theory and Methods Used

This chapter will present how solids are modeled using Bloch's theorem as well as how spin-orbit coupling is considered. Density functional theory and the pseudopotential environment used in the electronic and structural calculations is also included. This discussion involves a description of the Kohn-Sham formalism, exchange-correlation energy and the approximations used in this thesis. Following this is a description of the Becke-Johnson method and its advantages in calculating eigenvalues. Lastly, the family of Hall effects and their relationship to topological insulators is summarized and discussed.

2.1 Modeling Crystals: Bloch's Theorem, Spin-Orbit Coupling and Taking Advantage of Periodicity

Typically, crystals are described by a lattice, a set of primitive translation vectors: $\boldsymbol{a_1}$, $\boldsymbol{a_2}$, and $\boldsymbol{a_3}$ which generate the periodic system, and a basis, the unit cell which contains the atom position(s), $\boldsymbol{\tau_i}$, to be repeated across the lattice. We can then find the position of any

lattice point using a crystal translation vector, $\boldsymbol{T}$, of the form,

$$\boldsymbol{T} = u_1\boldsymbol{a_1} + u_2\boldsymbol{a_2} + u_3\boldsymbol{a_3} \tag{2.1}$$

where where u_1, u_2, u_3 are integers. The combination of these two sets of information (a lattice and a basis) can then be used to describe a crystal which repeats itself in all directions.

Another useful concept when examining condensed matter systems is the reciprocal lattice. This lattice is composed of primitive reciprocal lattice vectors of the form,

$$\begin{aligned}
\boldsymbol{b_1} &= 2\pi\frac{\boldsymbol{a_2}\times\boldsymbol{a_3}}{\boldsymbol{a_1}\cdot\boldsymbol{a_2}\times\boldsymbol{a_3}} \\
\boldsymbol{b_2} &= 2\pi\frac{\boldsymbol{a_3}\times\boldsymbol{a_1}}{\boldsymbol{a_1}\cdot\boldsymbol{a_2}\times\boldsymbol{a_3}} \\
\boldsymbol{b_3} &= 2\pi\frac{\boldsymbol{a_1}\times\boldsymbol{a_2}}{\boldsymbol{a_1}\cdot\boldsymbol{a_2}\times\boldsymbol{a_3}}.
\end{aligned} \tag{2.2}$$

where $\boldsymbol{A}\times\boldsymbol{B}$ and $\boldsymbol{A}\cdot\boldsymbol{B}$ denote the cross and dot-product of two vectors. Additionally, in the same way a translation vector $\boldsymbol{T}$ can be defined to point to any lattice point, a reciprocal translation vector, $\boldsymbol{G}$ can be defined as

$$\boldsymbol{G} = v_1\boldsymbol{b_1} + v_2\boldsymbol{b_2} + v_3\boldsymbol{b_3}, \tag{2.3}$$

where v_1, v_2, v_3 are integers.

This concept arises when considering periodic functions within the material, such as the electron density. Using a periodic quantity such as this provides an excellent environment for a Fourier analysis. In three dimensions we can write the density $n(\boldsymbol{r})$ in terms of a set of vectors $\boldsymbol{G}$ such that

$$n(\boldsymbol{r}) = \sum_{\boldsymbol{G}} n_{\boldsymbol{G}} e^{i\boldsymbol{G}\cdot\boldsymbol{r}}. \tag{2.4}$$

The vectors, $\boldsymbol{G}$, then, are reciprocal lattice vectors which conjugate the real space lattice to

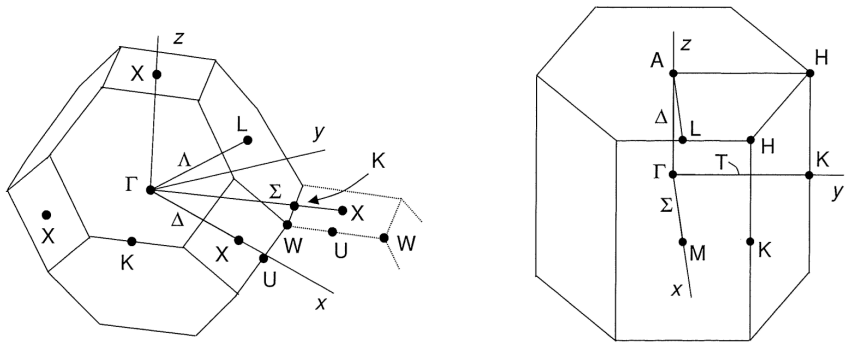

(a) (b)

Figure 2.1: Brillouin zones for (a) a face centered cubic (fcc) lattice and (b) a hexagonal lattice. Special points are labeled with the zone center designated as Γ. Figure taken from [3].

reciprocal or k-space. It is then useful to consider the Wigner-Seitz cell of this reciprocal lattice, known as the first Brillouin zone (known simply as the "Brillouin zone" or BZ). This cell is defined by planes that are perpendicular bisectors of the vectors from the origin to the reciprocal lattice points, and examples of these cells are shown in Figure 2.1.

Since everything within our solid is constructed using periodic functions, we can utilize the Bloch theorem. This theorem provides a powerful tool for describing the wavefunctions of electrons moving through a solid state system and states:

> The eigenfunctions of the wave equation for a periodic potential are the product of a plane wave $\exp(i\boldsymbol{k}\cdot\boldsymbol{r})$ times a functions $u_{\boldsymbol{k}}(\boldsymbol{r})$ with the periodicity of the crystal lattice [5].

This provides us with the form for solutions to the Schrödinger equation:

$$\psi_{n\boldsymbol{k}} = u_{n\boldsymbol{k}}(\boldsymbol{r})e^{i\boldsymbol{k}\cdot\boldsymbol{r}} \tag{2.5}$$

where $\boldsymbol{k}$ is the wave vector, n is the electron band number, and $u_{n\boldsymbol{k}}(\boldsymbol{r})$ is a function that has the period of the crystal lattice. We will explore this solution futher after introducing the plane-wave basis in Section 2.2.

Relativistic effects also become enormously important to consider when modeling systems with heavy atoms such as Sn. This is because the core electrons begin to approach relativistic speeds due to the stronger coulomb attraction of the massive nucleus. Within the core, these effects are considered in one of two ways: a scalar relativistic equation and a fully relativistic equation (given in [3]). These equations are derived from the Dirac equation describing the Hamiltonian

$$\hat{H}_{Rel} = c\boldsymbol{\alpha} \cdot \boldsymbol{p} + \beta mc^2 + V \tag{2.6}$$

where $\boldsymbol{p}$ is the usual momentum operator ($\boldsymbol{p} = -i\hbar\nabla$), V is the external potential, and $\boldsymbol{\alpha}$ and β are (4x4) matrices described as

$$\boldsymbol{\alpha} = \begin{pmatrix} 0 & \boldsymbol{\sigma} \\ \boldsymbol{\sigma} & 0 \end{pmatrix}, \qquad \beta = \begin{pmatrix} \boldsymbol{I} & 0 \\ 0 & -\boldsymbol{I} \end{pmatrix}, \tag{2.7}$$

where $\boldsymbol{I}$ is the (2x2) identity matrix and $\boldsymbol{\sigma}$ are the (2x2) Pauli spin matrices

$$\sigma_1 = \begin{pmatrix} 0 & 1 \\ 1 & 0 \end{pmatrix}, \qquad \sigma_2 = \begin{pmatrix} 0 & -i \\ i & 0 \end{pmatrix}, \qquad \sigma_3 = \begin{pmatrix} 1 & 0 \\ 0 & -1 \end{pmatrix}. \tag{2.8}$$

When this Hamiltonian is used within the Schrödinger equation, we get an expression of the form [31]

$$\left[\frac{p^2}{2m} + V - \frac{p^4}{8mc^2} + \frac{\hbar}{4m^3c^2}(\nabla V \cdot \boldsymbol{p}) + \frac{\hbar}{4m^2c^2}(\nabla V \times \boldsymbol{p}) \cdot \boldsymbol{\sigma}\right] \Psi = E\Psi. \tag{2.9}$$

The first two terms here are the usual non-relativistic parts of the Schrödinger equation, the third term is the first-order relativistic correction for an electron moving at high speeds, and the fourth term is a small contribution to the total energy known as the Darwin term. The last term is the energy contribution to spin-orbit coupling (SOC), which, in the presence of

a spherically symmetric Coulomb potential, takes the familiar form

$$\frac{\hbar^2}{4m^2c^2}\frac{1}{r}\frac{\partial V}{\partial r}\boldsymbol{l}\cdot\boldsymbol{s}. \tag{2.10}$$

The scalar relativistic equation ignores this spin-orbit coupling term, since its contribution to the energy is usually small, while the fully relativistic equation will take this term into account.

In this thesis, our models will first ignore SOC (while still considering other relativistic effects) and then consider SOC in order to evaluate its effects. Spin-orbit coupling will be considered in two ways. The first is to utilize the fully relativistic wave equation during pseudopotential generation (explained in more detail in Section 2.3 and 3.1). The second is to make the valence electron wave functions a spinor, rather than a scalar function. Storing the spin information into the wave function has been shown to break degeneracies in band structure calculations [32] and, in fact, can induce a band gap in monolayer stanene (Ch. 4).

2.2 Density Functiontal Theory

The careful imagining of a material requires the consideration of a collection of nuclei, the electrons surrounding them, and the interactions between each particle. If one is to predict the physical properties of a material, we must begin thinking about a very large collection of these particles, which quickly becomes very difficult to calculate. Fortunately however, simplifications can be made. We begin by first considering the much more massive nuclei as being stationary compared to the fast-moving electrons, known as the Bohr-Oppenheimer approximation [33]. This allows us to interpret the system as many free electrons moving around in a constant, periodic potential. With this first approximation in mind, we can begin to consider the ground state total energy; allowing for the prediction of other properties such as lattice constants, bond lengths, binding energies, and electronic structure.

In order to construct the Hamiltonian, we must consider a kinetic energy term and

three potential energy terms arising from the interactions of: nuclei between nuclei, electrons between nuclei, and the interaction of electrons between electrons

$$\hat{H} = \hat{T} + \hat{V}_{ee} + \hat{V}_{ext}. \tag{2.11}$$

The last term, V_{ext}, contains the coulomb interactions of nuclei between nuclei and electrons between nuclei given by

$$\hat{V}_{ext} = \hat{V}_{el-nuc} + \hat{V}_{nuc-nuc} = -\sum_i \sum_a \frac{Z_a}{|\mathbf{r}_i - \mathbf{R}_a|} + \sum_{i \neq j} \frac{Z_i Z_j}{R_{ij}}, \tag{2.12}$$

the electron-electron Coulomb repulsion is

$$\hat{V}_{ee} = \frac{1}{2} \sum_{i \neq j} \frac{1}{|\mathbf{r}_i - \mathbf{r}_j|}, \tag{2.13}$$

and the kinetic energy term is

$$\hat{T} = -\frac{1}{2} \sum_{i=1}^{N} \nabla_i^2. \tag{2.14}$$

Here $\mathbf{r}_i$ and $\mathbf{r}_j$ are electron positions, $\mathbf{R}_a$ is the nuclear position and Z_a is the atomic number of that nucleus. (To quickly avoid confusion, note that these expressions use atomic units which set $e^2 = \hbar = 4\pi\epsilon_0 = m_e = 1$).

2.2.1 Hohenberg-Kohn Theorems

However, these expressions are useful only for a system of N particles. This proves to be enormously difficult to compute as we begin to imagine a system with 10^{23} particles. Fortunately, we can turn this many-body problem into a single-body problem that depends solely upon an average ground state electron density $n(\boldsymbol{r})$, known as the Hohenberg-Kohn theorems [34]. The first of these theorems states that for any system of interacting paricles, the external potential, $V_{ext}(\boldsymbol{r})$, is uniquely determined by the ground state density $n(\boldsymbol{r})$, save

for a constant (in our case, this is the Coulombic nuclei-nuclei interactions). It then follows that, since the Hamiltonian is fully determined, the many-body wave functions for all states are determined. Thus, all properties of the system are completly determined if given only the ground state density, $n(\boldsymbol{r})$.

The second theorem states that a universal functional for the energy of the system, $E[n]$, can be defined in terms of the ground state density, $n(\boldsymbol{r})$

$$E[n] = \langle \Psi_0[n] | \, \hat{T} + \hat{V}_{ee} + \hat{V}_{ext} \, | \Psi_0[n] \rangle \, . \tag{2.15}$$

Here Ψ_0 is the ground state wave function that is associated with the ground state density, n. Then, since the many-body wave functions are determined by the density, we can define the total energy as

$$E[n] = \langle \hat{T} \rangle + \langle \hat{V}_{ee} \rangle + \langle \hat{V}_{ext} \rangle = T[n] + U_{ee}[n] + U_{ext}[n]. \tag{2.16}$$

We have now reduced the many-body problem to depend on just a single quantity! In addition, the expectation, $\langle \hat{V}_{ext} \rangle$, can be exactly calculated using the density via the relation:

$$\langle \hat{V}_{ext} \rangle = U_{ext} = \int d\boldsymbol{r} V_{ext}(\boldsymbol{r}) n(\boldsymbol{r}). \tag{2.17}$$

However, the potential term U_{ee} is still an unknown which proves to be quite difficult to solve for an interacting electron system.

2.2.2 Kohn-Sham Theorems

The crux of density functional theory's usefulness lies in the proceeding work by Kohn and Sham [35]. The approach is this: to replace the original, difficult-to-solve, interacting particle Hamiltonian with that of a *fake*, non-interacting particle Hamiltonian. This replacement relies on the Kohn-Sham ansatz which is based off of two primary assumptions:

1. The exact ground state density can be repesented by the ground state density of an auxiliary system of non-interacting particles.
2. This auxiliary Hamiltonian is choosen to have the usual kinetic energy operator and an effective local potential $V_{eff}^{\sigma}(\boldsymbol{r})$ which acts upon an electron of spin σ at a point $\boldsymbol{r}$.

The Hamiltonian of this new, auxiliary system is then given by

$$\hat{H}_{aux} = -\frac{1}{2}\nabla^2 + \hat{V}_{eff}^{\sigma}. \tag{2.18}$$

The density of this auxiliary system is simply the sum over the probabilities of the electron orbitals at a point $\boldsymbol{r}$,

$$n(\boldsymbol{r},\sigma) = \sum_{\sigma}\sum_{i}^{N^{\sigma}} |\psi_i^{\sigma}(\boldsymbol{r})|^2, \tag{2.19}$$

and the kinetic energy of this system, T_s, is then

$$T_s = -\frac{1}{2}\sum_{\sigma}\sum_{i=1}^{N^{\sigma}} \langle\psi_i^{\sigma}|\,\nabla^2\,|\psi_i^{\sigma}\rangle = \frac{1}{2}\sum_{\sigma}\sum_{i=1}^{N^{\sigma}} |\nabla\psi_i^{\sigma}|^2. \tag{2.20}$$

In addition, the Coulombic energy of the electron density interacting with itself is included as

$$U_{Hartree}[n] = \frac{1}{2}\int\int d^3r d^3r' \frac{n(\boldsymbol{r})n(\boldsymbol{r}')}{|\boldsymbol{r}-\boldsymbol{r}'|}, \tag{2.21}$$

which allowed Kohn and Sham to express the energy of the system in the form

$$E_{KS}[n] = T_s[n] + \int d\boldsymbol{r} V_{ext}(\boldsymbol{r})n(\boldsymbol{r}) + U_{Hartree}[n] + U_{II} + E_{XC}[n], \tag{2.22}$$

where $V_{ext}(\boldsymbol{r})$ is the external potential due to the nuceli and U_{II} is the interaction energy between nuclei. The last term, $E_{XC}[n]$, groups the complicated, many-body effects of exchange and correlation together into a single term, known as the exchange-correlation (XC) energy. If we compare this expression for total energy with that of the total energy of the

true electron system, E_{XC} can be written in terms of Eq. 2.16 and 2.22 as

$$E_{XC}[n] = (T[n] - T_s[n]) + (U_{ee}[n] - U_{Hartree}[n]), \tag{2.23}$$

that is, the difference between the kinetic and electron-electron interaction energy of the real system ($T[n]$ and $U_{ee}[n]$) and the fake, non-interacting system ($T_s[n]$ and $U_{Hartree}[n]$).

Thus, if the universal functional, E_{XC}, were known, then the exact ground state energy and density of the original many-body electron problem could be found by solving the Kohn-Sham equations. Unfortunaley, the true form of this functional has proven to be notoriously difficult to find and so approximations of this energy must be made. However, these approximations provide a feasible approach to calculating the ground state properties and the Kohn-Sham energy can be minimized (and therefore solved for the ground state) through the calculus of variations.

2.2.3 Utilizing the Calculus of Variations

The solution of Eq. 2.22 for the ground state of the auxiliary system can be viewed as a problem of minimization with respect to the density $n(\boldsymbol{r}, \sigma)$. Since T_s is written explicity in terms of the orbital wavefunctions, we can take the functional derivative of E_{KS} with respect to the orbitals and utilize the chain rule to write the functional derivative with respect to the density for the other terms. This takes the form

$$\frac{\delta E_{KS}}{\delta \psi_i^{\sigma *}(\boldsymbol{r})} = \frac{\delta T_s}{\delta \psi_i^{\sigma *}(\boldsymbol{r})} + \left[\frac{\delta U_{ext}}{\delta n(\boldsymbol{r}, \sigma)} + \frac{\delta U_{Hartree}}{\delta n(\boldsymbol{r}, \sigma)} + \frac{\delta E_{XC}}{\delta n(\boldsymbol{r}, \sigma)} \right] \frac{\delta n(\boldsymbol{r}, \sigma)}{\delta \psi_i^{\sigma *}(\boldsymbol{r})} = 0, \tag{2.24}$$

which is subject to the normalization condition

$$\langle \psi_i^{\sigma}(\boldsymbol{r}) | \, | \psi_j^{\sigma}(\boldsymbol{r}) \rangle = \delta_{i,j} \delta_{\sigma,\sigma'}. \tag{2.25}$$

The first term in Eq. 2.24 is then the kinetic energy term of the Hamiltonian

$$\frac{\delta T_s}{\delta \psi_i^{\sigma *}(\boldsymbol{r})} = -\frac{1}{2}\nabla^2 \Psi_i^{\sigma}(\boldsymbol{r}), \tag{2.26}$$

and the chain rule derivative is,

$$\frac{\delta n(\boldsymbol{r}, \sigma)}{\delta \psi_i^{\sigma *}(\boldsymbol{r})} = \psi_i^{\sigma}(\boldsymbol{r}). \tag{2.27}$$

Then, armed with the method of Lagrange multipliers, we can express an effective Kohn-Sham Hamiltonian, $\hat{H}_{KS}$,

$$\hat{H}_{KS}^{\sigma} = -\frac{1}{2}\nabla^2 + V_{KS}^{\sigma}(\boldsymbol{r}), \tag{2.28}$$

where

$$\begin{aligned} V_{KS}^{\sigma}(\boldsymbol{r}) &= V_{ext}(\boldsymbol{r}) + \frac{\delta U_{Hartree}}{\delta n(\boldsymbol{r}, \sigma)} + \frac{\delta E_{XC}}{\delta n(\boldsymbol{r}, \sigma)} \\ &= V_{ext}(\boldsymbol{r}) + V_{Hartree}(\boldsymbol{r}) + V_{XC}^{\sigma}(\boldsymbol{r}). \end{aligned} \tag{2.29}$$

This effective Hamiltonian can then be used in a Schrödinger-like equation which takes the form

$$\hat{H}_{KS}^{\sigma}\psi_i^{\sigma}(\boldsymbol{r}) = \epsilon_i \psi_i^{\sigma}(\boldsymbol{r}) \Rightarrow (\hat{H}_{KS}^{\sigma} - \epsilon_i)\psi_i^{\sigma}(\boldsymbol{r}) = 0. \tag{2.30}$$

The orbital wave function, $\psi_i^{\sigma}(\boldsymbol{r})$, *cannot* be zero, and so it is the term in parentheses that must satisfy this condition. Effectively, this causes Eq. 2.30 to take the form

$$-\frac{1}{2}\nabla^2\psi_i^{\sigma}(\boldsymbol{r}) + V_{ext}(\boldsymbol{r})\psi_i^{\sigma}(\boldsymbol{r}) + V_{Hartree}(\boldsymbol{r})\psi_i^{\sigma}(\boldsymbol{r}) + V_{XC}^{\sigma}(\boldsymbol{r})\psi_i^{\sigma}(\boldsymbol{r}) - \epsilon_i\psi_i^{\sigma}(\boldsymbol{r}) = 0. \tag{2.31}$$

The only term that remains unknown here is $V_{XC}^{\sigma}(\boldsymbol{r})$, known as the exchange-correlation potential. This term, along with $E_{XC}[n]$, is where the DFT community diverges; since these terms must be approximated, which approximation is the correct one? For the sake of brevity, this thesis will only examine the approximations used in this work. A discussion and analysis of the effectiveness for several of these approximations can be found in [3], [36],

and [37].

2.2.4 Approximating the Exchange-Correlation Energy

The XC energy, as previously mentioned, is an additional term which ensures that the non-interacting, auxiliary system provides the ground state energy of the true, interacting system. Specifically, Eq. 2.23 demonstrates that this energy is simply that of the difference in kinetic and internal interaction energies between the real and the auxiliary system. It follows then, that the XC energy gives additional information about the real system that was lost through the auxiliary system's approximation of a non-interacting electron density.

Furthermore, the XC energy is actually two separate types of interaction energies which are contained in this term. These energies are: E_X, the exchange energy due to the Pauli exclusion principle, and E_C, the correlation energy which is due to the Coulombic interaction between electrons

$$E_{XC}[n] = E_X[n] + E_C[n]. \tag{2.32}$$

Note that this is a static energy; meaning that within this system, all the electrons will shift in relation to one another in order to minimize their interaction energies until the total energy is minimized. The approximations this thesis uses for the XC energy are the generalized gradient approximattion (GGA) and a meta-generalized gradient approximation (m-GGA), known as the Becke-Johnson (BJ) method and are described below.

Generalized Gradient Approximation

The most simplistic approximation for the XC energy we can make is based on the assumption that the system possesses a slowly varying electron density. This assumption (known as the local density approximation) allows us to treat the density at any point in space as that of a homogeneous electron gas. The generalized gradient approximation (GGA) attempts

to improve upon this by considering the gradient of this slowly varying density, as well as the density itself. The XC energy for the GGA is simply an integral over all space with an exchange-correlation energy density, ϵ_{xc}, which can be split into an exchange energy density, ϵ_x, and a correlation energy density ϵ_c,

$$E_{xc}^{GGA}[n] = \int d^3r n(\boldsymbol{r})\epsilon_{xc} = \int d^3r n(\boldsymbol{r})[\epsilon_x + \epsilon_c] \tag{2.33}$$

The exchange energy density for a GGA is then given the form

$$\epsilon_x = F_x(s^2)\epsilon_x^{HEG}. \tag{2.34}$$

Here, ϵ_x^{HEG} is the exchange energy of a homogeneous electron gas and $F_x(s^2)$ is the exchange scaling factor, dependent on s, which is related to the gradient of the density by

$$s = \frac{|\nabla n|}{2k_f n}, \tag{2.35}$$

where k_f is the fermi wave vector of the homogeneous electron gas, $k_f = (3\pi^2 n)^{\frac{1}{3}}$. The energy density of the homogeneous electron gas, meanwhile, is expressed as

$$\epsilon_x^{HEG} = -\frac{3}{4\pi}\left(\frac{9\pi}{4}\right)^{\frac{1}{3}}\left(\frac{3}{4\pi n}\right)^{-\frac{1}{3}}. \tag{2.36}$$

The correlation energy is a bit more difficult to cast as a general functional, so we will use the Perdew-Burke-Ernzerhof (PBE) correlation functional [38] as an example. This functional starts from the simple approximation of a homogeneous electron gas, and adds a gradient-based term given by

$$E_c^{PBE} = \int d^3r n\left[\epsilon_c^{HEG}(r_s,\zeta) + H(r_s,\zeta,t)\right]. \tag{2.37}$$

Here, r_s is the Wigner-Seitz radius of homogeneous electron gas given by

$$r_s = \left(\frac{3}{4\pi n}\right)^{\frac{1}{3}}, \tag{2.38}$$

ζ is a measure of the relative spin polarization

$$\zeta = \frac{(n_\uparrow + n_\downarrow)}{n}, \tag{2.39}$$

and t is a dimensionless quantity related to the gradient of the density

$$t = \frac{|\nabla n|}{2\phi k_s n}. \tag{2.40}$$

The term, ϕ, is a spin scaling factor $\phi = \left[(1+\zeta)^{\frac{2}{3}} + (1-\zeta)^{\frac{2}{3}}\right]/2$ and $k_s = (4\pi e^2 n)/\epsilon_0$ is the Thomas-Fermi screening length.

It is important to note here that this thesis uses the PBEsol XC functional [39], which, like the PBE functional, handles the two coefficients controlling the strength of the gradient correction for exchange and correlation separately. This modified version of the PBE functional was chosen to be used for structural investigations because it has been shown to yield better physical parameters such as lattice constants and bulk modulii. However, when investigations of the electronic energy levels and excited states are considered, PBEsol falls short. A different functional to handle exchange energies is then utilized which is described below.

Becke-Johnson Method

The PBE and PBEsol XC functionals were constructed to generate accurate XC energies; however, these functionals tend to generate poor XC potentials. This leads to an accurate ground state energy, but poor eigenvalues when solving Eq. 2.31. If we only consider the ground state of a system, this issue does not prove to be terribly problematic. However,

once investigations of anything involving the excited states of a system are considered, this becomes a problem. To alleviate this, a method which can provide accurate eigenvalues without becoming too computationally expensive must be found. One such approximation, which is used in this thesis, is the Becke-Johnson method which modifies the exchange potential while using the same GGA correlation potential as above. This exchange potential moves a step beyond the traditional GGA and considers the Laplacian of the density and the kinetic energy density, in addition to the gradient.

Becke and Johnson [40] designed an exchange potential which makes a practical approximation of the optimized effective potential (OEP). First introduced by Sharp and Horton [41] and Talman and Shadwick [42], the OEP is a method to find the exact Kohn-Sham potential, V_{KS}. The problem, however is that the integral equation for the OEP is difficult to solve. Becke and Johnson proposed an exchange potential that acts as a correction to the Slater potential [43]

$$V_{x,\sigma}^{Slater}(\boldsymbol{r}_1) = -\int \frac{\rho_{X,\sigma}(\boldsymbol{r}_1, \boldsymbol{r}_2)}{r_{12}} d^3\boldsymbol{r}_2, \tag{2.41}$$

where $\rho_{X,\sigma}$ is the density of an exchange "hole" given by

$$\rho_{X,\sigma}(\boldsymbol{r}_1, \boldsymbol{r}_2) = \frac{1}{n_\sigma(\boldsymbol{r}_1)} \left| \sum_i \psi_{i\sigma}^*(\boldsymbol{r}_1)\psi_{i\sigma}(\boldsymbol{r}_2) \right|^2 . \tag{2.42}$$

The proposed BJ exchange potential is then

$$V_{x,\sigma}^{BJ} = V_{x,\sigma}^{Slater} + C_{\Delta V}\sqrt{\frac{\tau_\sigma}{n_\sigma}}, \tag{2.43}$$

where

$$C_{\Delta V} = \frac{1}{\pi}\sqrt{\frac{5}{12}} \tag{2.44}$$

and τ_σ is the kinetic energy density of electrons with spin σ

$$\tau_\sigma = \sum_i |\nabla\psi_{i\sigma}|^2. \tag{2.45}$$

Unfortunately however, since this is only an exchange potential and not an exchange *energy*, it is not possible to use this potential to find the ground state parameters of a system. Thus, this thesis will use the GGA functional PBEsol to find the ground state energy, electron density, and associated eigenvalues. The BJ method will then be used as a *correction* for these eigenvalues in order to predict a more accurate electronic structure.

2.3 Technical Implementation

This information provides us with everything we need to begin modeling our solid. The procedure then, is to solve the KS equation(Eq. 2.31), calculate eigenvalues for various values of k, and then use this information to calculate the ground state energy and associated ground state quantities. We use the coding package, ABINIT [57], [58], for the calculations within this thesis. This package uses the plane wave pseudopotential method which is described below.

DFT methods for describing crystals use an iterative process known as a self-consistent field (SCF) calculation to approximate the solution for the density. This process is composed of five primary steps which are shown in Figure 2.2. The first step is to make an educated guess of the ground state electron density. Next, the effective potential is calculated using this density to solve Eq. 2.29. The V_{XC} term contains all relevant information about the XC functional being used. Following this, the effective potential, V_{KS}, is placed into the Kohn-Sham Hamiltonian (Eq. 2.30), at which point Eq. 2.31 can be solved, providing the wavefunctions associated with this density. These wavefunctions are then used to calculate a new density using Eq. 2.19. If this new density is equal to the initial guessed density to within some tolerance, the cycle is finished and the ground state parameters of the system can be solved for. If not, then this new density replaces the old density and the process is repeated.

Within a plane-wave pseudopotential code, we require states to obey periodic bound-

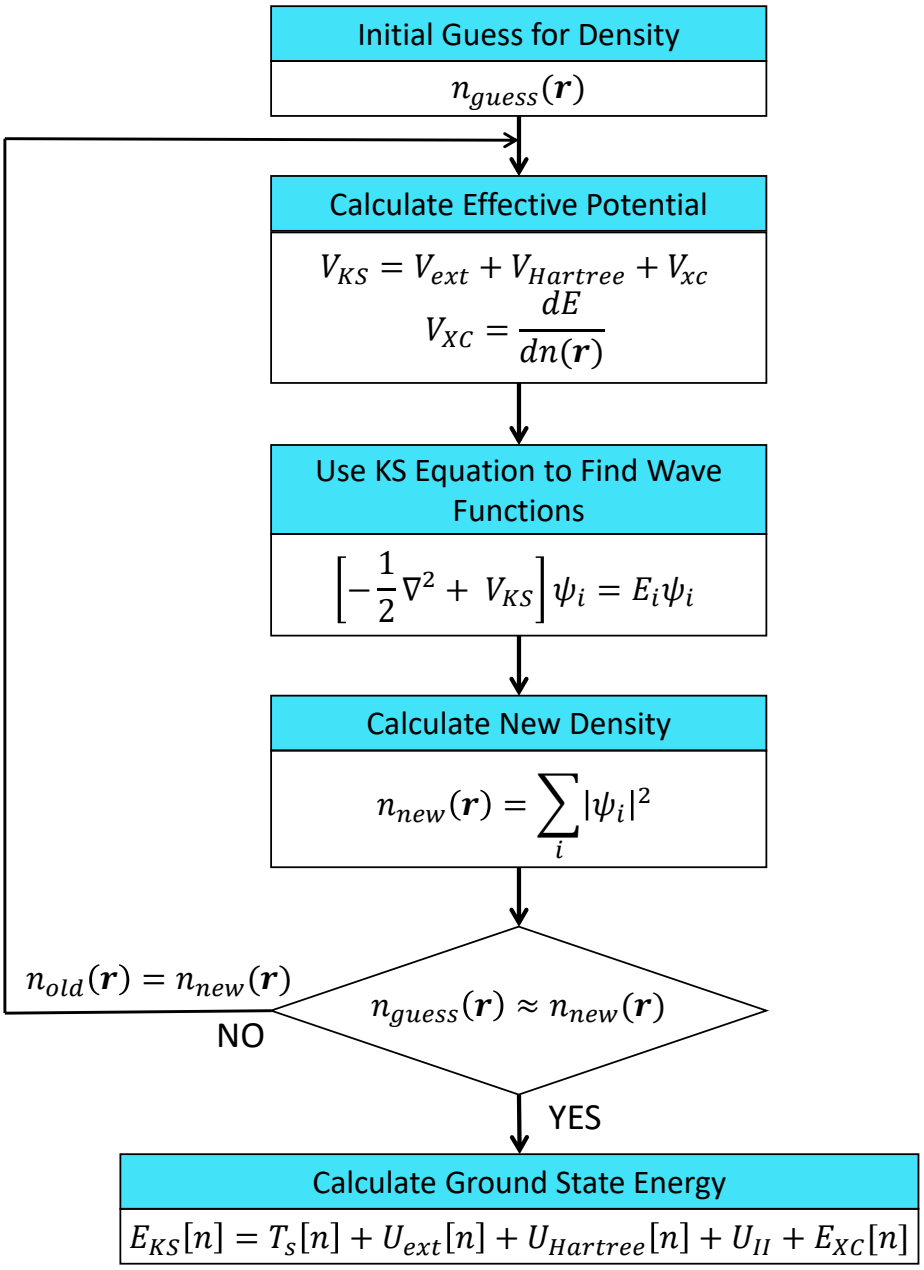

Figure 2.2: Flowchart demonstrating the details of the SCF calculation used within the ABINIT software package.

ary conditions (in addition to being normalized) within some large volume Ω. Within this system, an eigenfunction can be written as

$$\psi_i(\boldsymbol{r}) = \sum_{\boldsymbol{q}} c_{i,\boldsymbol{q}} \frac{e^{i\boldsymbol{q}\cdot\boldsymbol{r}}}{\sqrt{\Omega}} \equiv \sum_{\boldsymbol{q}} c_{i,\boldsymbol{q}} \left|\boldsymbol{q}\right\rangle, \tag{2.46}$$

where $c_{i,\boldsymbol{q}}$ are expansion coefficients of the wave function in a basis of orthonormal plane waves $\left|\boldsymbol{q}\right\rangle$ satisfying

$$\left\langle \boldsymbol{q}' \right| \left|\boldsymbol{q}\right\rangle \equiv \frac{1}{\Omega} \int_{\Omega} d^3r \; e^{-i\boldsymbol{q}'\cdot\boldsymbol{r}} e^{i\boldsymbol{q}\cdot\boldsymbol{r}} = \delta_{\boldsymbol{q}',\boldsymbol{q}}. \tag{2.47}$$

If we insert this into Eq. 2.28 and multiply from the left by $\left\langle \boldsymbol{q}' \right|$ we get

$$\sum_{\boldsymbol{q}} \left\langle \boldsymbol{q}' \right| \hat{H}_{KS} \left|\boldsymbol{q}\right\rangle = \sum_{\boldsymbol{q}} \left\langle \boldsymbol{q}' \right| -\frac{1}{2}\nabla^2 + V_{KS}(\boldsymbol{r}) \left|\boldsymbol{q}\right\rangle = \epsilon_i \sum_{\boldsymbol{q}} \left\langle \boldsymbol{q}' \right| \left|\boldsymbol{q}\right\rangle c_{i,\boldsymbol{q}} = \epsilon_i c_{i,\boldsymbol{q}} \tag{2.48}$$

(for the sake of concision, the spin term σ is ignored here). The kinetic energy term is then simply

$$\left\langle \boldsymbol{q}' \right| -\frac{1}{2}\nabla^2 \left|\boldsymbol{q}\right\rangle = \frac{1}{2}|q|^2 \delta_{\boldsymbol{q}',\boldsymbol{q}}. \tag{2.49}$$

Additionally, for a crystal, the potential $V_{KS}(\boldsymbol{r})$ is periodic and so can be expressed as a sum of Fourier components

$$V_{KS}(\boldsymbol{r}) = \sum_{m} V_{KS}(\boldsymbol{G}_m) e^{-i\boldsymbol{G}_m\cdot\boldsymbol{r}} \tag{2.50}$$

where m is an integer, $\boldsymbol{G}_m$ are reciprocal lattice vectors, and $V_{KS}(\boldsymbol{G}_m)$ is defined as

$$V_{KS}(\boldsymbol{G}) = \frac{1}{\Omega_{cell}} \int_{\Omega_{cell}} V_{KS}(\boldsymbol{r}) e^{-i\boldsymbol{G}\cdot\boldsymbol{r}} d\boldsymbol{r}, \tag{2.51}$$

where Ω_{cell} is the volume of the primitive unit cell. The potential then takes the form

$$\left\langle \boldsymbol{q}' \right| V_{KS} \left|\boldsymbol{q}\right\rangle = \sum_{m} V_{KS}(\boldsymbol{G}_m) \delta_{\boldsymbol{q}'-\boldsymbol{q},\boldsymbol{G}_m}, \tag{2.52}$$

which requires that $\boldsymbol{q}$ and $\boldsymbol{q}'$ differ by some reciprocal lattice vector $\boldsymbol{G}_m$. Lastly, if we define

$\boldsymbol{q} = \boldsymbol{k} + \boldsymbol{G}_m$ and $\boldsymbol{q}' = \boldsymbol{k} + \boldsymbol{G}_{m'}$ (where $\boldsymbol{G}_m$ and $\boldsymbol{G}_{m'}$ differ by a reciprocal lattice vector), we can then write the Schrödinger equation for any given $\boldsymbol{k}$ within this plane-wave basis

$$\sum_{m'} H_{m,m'}(\boldsymbol{k}) c_{i,m'}(\boldsymbol{k}) = \epsilon_i(\boldsymbol{k}) c_{i,m}(\boldsymbol{k}), \tag{2.53}$$

where

$$\begin{aligned} H_{m,m'}(\boldsymbol{k}) &= \langle \boldsymbol{k} + \boldsymbol{G}_m | -\frac{1}{2}\nabla^2 + V_{KS}(\boldsymbol{r}) \, | \boldsymbol{k} + \boldsymbol{G}_{m'} \rangle \\ &= \frac{1}{2}|\boldsymbol{k} + \boldsymbol{G}_m|^2 \delta_{m,m'} + V_{KS}(\boldsymbol{G}_m - \boldsymbol{G}_{m'}). \end{aligned} \tag{2.54}$$

Our eigenfunction (written in terms of $\boldsymbol{q}$) can now be written in terms of any given wave vector, $\boldsymbol{k}$ as

$$\begin{aligned} \psi_{i,\boldsymbol{k}}(\boldsymbol{r}) &= \frac{1}{\sqrt{\Omega}} \sum_m c_{i,m}(\boldsymbol{k}) e^{i(\boldsymbol{k}+\boldsymbol{G}_m)\cdot\boldsymbol{r}} \\ &= \frac{1}{\sqrt{N_{cell}}} u_{i,\boldsymbol{k}}(\boldsymbol{r}) e^{i\boldsymbol{k}\cdot\boldsymbol{r}} \end{aligned} \tag{2.55}$$

where

$$u_{i,\boldsymbol{k}} = \frac{1}{\sqrt{\Omega_{cell}}} \sum_m c_{i,m}(\boldsymbol{k}) e^{i\boldsymbol{G}_m\cdot\boldsymbol{r}} \tag{2.56}$$

and $\Omega = N_{cell}\Omega_{cell}$. This is essentially a restatement of Bloch's theorem. Any eigenfunction in a periodic system is a product of $e^{i\boldsymbol{k}\cdot\boldsymbol{r}}$ and some peiodic function $u_{i,\boldsymbol{k}}$. Note that, in the limit of large Ω, the eigenvalues, $\epsilon_i(\boldsymbol{k})$, move from being discrete sets of values into continuous *bands* which are denoted by the index i (i.e. at each $\boldsymbol{k}$, there are a discrete set of eigenstates labeled $i = 1, 2, 3....$). Lastly, the density in Eq. 2.19 then takes the form of a summation over these bands integrated over all k-space

$$n(\boldsymbol{r}) = \sum_i \int \frac{d^3k}{(2\pi)^3} |u_{i,\boldsymbol{k}}(\boldsymbol{r})|^2. \tag{2.57}$$

Additionally, it follows from our Scrödinger equation that the solutions are periodic

in $\boldsymbol{k}$ such that all unique solutions are given by $\boldsymbol{k}$'s which are inside the primitive cell of the reciprocal lattice. The best choice for this cell is the first Brillouin zone since it is the most compact, uniquely defined cell in reciprocal space. It is then useful for computational implementation for the k-space integral to be over the volume of the first BZ. Its boundaries are defined by the bisecting planes of the $\boldsymbol{G}$ vectors and ensures that any wave vector, $\boldsymbol{k}$, outside of this cell can be related to a $\boldsymbol{k}'$ within the cell using the relation

$$\boldsymbol{k}' + \boldsymbol{G} = \boldsymbol{k}. \tag{2.58}$$

These plane-waves then define the basis with which we can describe our system.

However, when we consider electrons which orbit near the core, we run into a problem. These wavefunctions possess very rapid variation, making our plane-wave based system rather computationally difficult to describe. This is where the *pseudopotential* in "plane-wave pseudopotential method" comes in. A pseudopotential replaces the core electrons with that of an effective ionic potential acting on the valence electrons. This is accomplished using the frozen core approximation [44], and a discussion of the generation of the pseudopotentials used in this thesis can be found in Section 3.1. Additionally, a discussion of the general theory of pseudopotentials can be found in [3], [36], and [45].

The final remaining issue is that of the transposition of our plane-wave basis to that of a computational environment. Recall that the sums over m in Eqs. 2.50,2.53,2.55, and 2.56 all extend to infinity and that $\boldsymbol{G}_m$ obeys the relation

$$\boldsymbol{G}_m \cdot \boldsymbol{T} = 2\pi m, \tag{2.59}$$

where $\boldsymbol{T}$ is a translation vector in real space. Unfortunately, computers are not yet able to count to infinity, and so a cutoff $\boldsymbol{G}_m$ must be chosen. In the ABINIT environment this takes

the form of a cutoff energy for a given $\boldsymbol{k}$ with the relation

$$\frac{1}{2}|2\pi(\boldsymbol{k}+\boldsymbol{G}_{cut})|^2 = E_{cut}. \tag{2.60}$$

This cutoff solves the problem of the infinite sum, but the wave vector, $\boldsymbol{k}$ remains to be a continuous variable. To alleviate this, a finite grid of k points is created by choosing a super-lattice describing the system, the reciprocal of which provides a minimum spacing between k. The convergence of this minimum spacing and cutoff plane-wave energy as well as a further discussion of these discretizing techniques can be found in Section 3.2 and 4.1.2.

2.4 The Family of Hall Effects and Topological Insulators

Before the quantum-spin Hall effect (QSHE) can be described in detail, it is important to bring context to some of the members of the family of Hall effects: the Hall effect (HE), the quantum Hall effect (QHE), and the quantum-spin Hall effect. In addition, the relationship between the quantum-spin Hall effect and topological insulators will also be discussed.

The Hall effect, orginally discovered by Edwin H. Hall [46], arises when current, J_x, passes through a slab of conducting material that is placed within a perpendicular, external magnetic field B. The Lorentz force due to the movement of charge carriers within a magnetic field causes them to deflect toward one side of the material and accumulate along the edge. This induces a transverse electric field that is proportional to the current and magnetic field, known as the Hall field. An important relation between the external magnetic field, current, and Hall field was then defined as

$$R_{Hall} = \frac{E_{Hall}}{J_x B} \tag{2.61}$$

and is known as the Hall coefficient. For a two-dimensional sample of some width w, we know that $J_x = I/w$ and $E_{Hall} = V_{Hall}/w$ (where V_{Hall} is known as the Hall voltage) R_{Hall}

becomes

$$R_{Hall} = \frac{V_{Hall}}{IB}. \tag{2.62}$$

The quantum Hall effect (QHE) arises in low-temperature, two-dimensional electron systems subjected to strong magnetic fields and has been experimentally demonstrated in systems such as GaAs quantum wells [47]. To obeserve this we reverse the above experiment, applying a tranverse electric field E_y and measuring the longitudinal drift current J_d within the same orthogonal field, B. In this scenario, electrons are trapped in quantized cyclotron orbits known as Landau levels and the spacing between these levels is dependent upon the external magnetic field and effective mass of the electrons. Predicted by Ando *et al.* [48] and later experimentally observed by Klitzing *et. al.* [49], the QHE possesses states along the edge which can only travel clockwise or counterclockwise (dependent on the direction of the external field) with a quantized Hall conductance, σ_{xy} in units of e^2/h. These states are termed *chiral* and occur because the cyclotron orbits around the edge are broken due to edge collisions. This quantization also relates to the number of edge states this chiral drift current possesses. Meanwhile electrons in the bulk are trapped within closed orbits causing these states to be insulating (see Figure 2.3). The other striking feature of this effect is that the Hall conductance is *exactly* quantized in units of e^2/h [50] which has proven useful for accurate measurements of the fine structure constant [51].

The quantum-spin Hall effect (QSHE) can roughly be described as two, spin-dependent copies of the QHE due to spin-orbit coupling. Specifically, when relativistic effects becomes important, electrons will experience their own, internal magnetic field, inducing a QHE. The direction of this internal field is spin-dependent which separates the QHE into two edge states moving in opposite directions. These two helical edge states (Figure 2.3) are protected from backscattering, even though they are moving in opposite directions, because the direction of propogation is dependent upon spin. Further, in order to backscatter into an equal energy state, an electron must flip its spin, which requires time reversal symmetry to be broken.

To understand the Hall effect family's relationship to topology, it should be remem-

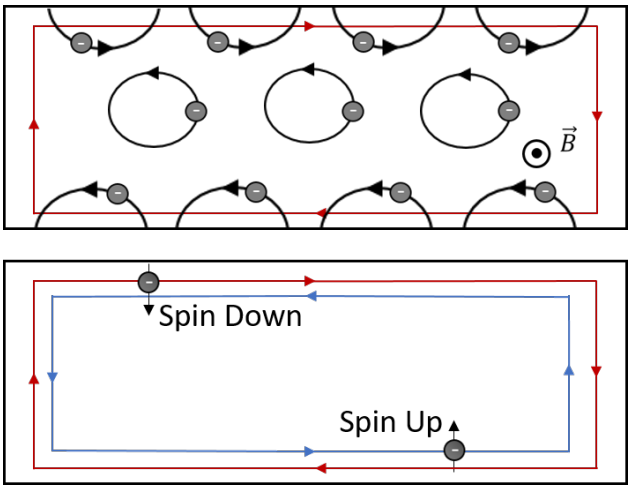

Figure 2.3: Schematic of the Quantum Hall Effect (top) and the Quantum Spin Hall Effect (bottom). A QHE is induced through an external magnetic field while a QSHE is induced through strong spin-orbit coupling in the presence of a system with tme-reversal symmetry.

bered how phases of condensed matter systems are classified, which, typically, is defined via the symmetries that they break. Classical liquids and gases, for example, enjoy translational and rotational symmetry, but a solid will break these symmetries to a handful of allowed tranlsations and rotations. These phases of matter are usually defined by a local order parameter while states such as the QHE and QSHE are characterized by a topological invariant. For the QHE, this invariant is known as the TKNN or Chern number and is related to the number of edge states [52]. For the QSHE however, a different topological invariant is used, known as the Z_2 invariant. One approach for this calculation is to measure the net parity of the valence bands at specific time reversal invariant momentum (TRIM) points in the BZ [53]. If the net parity of these bands is positive, then the topological state is trivial, and if the net parity is negative, the topological state in nontrivial and a QSH phase in present.

This field of topology as it relates to condensed matter systems is rather large and so a summation of this field would be too broad for the scope of this thesis. If interested in learning more about this burgeoning field, further reading can be found in [54], [55], and [56].

Chapter 3

Calculating Properties of Bulk Tin

The primary goal of this research is to investigate the electronic and structural properties of stanene using density functional theory (DFT) to calculate the total energy, charge density, and electronic structure. This is implemented using a plane-wave basis with a pseudopotential approximation. The code used provides a library of pseudopotentials, but none of them account for the effects of spin-orbit coupling, and so a pseudopotential that accounts for this must be generated. Following this, convergence parameters associated with our model are described and converged in order to ensure an appropriate accuracy in further calculations using a bulk α-Sn systems. Bulk tin is used for this step since there is little experimental data to be found for stanene itself and α-Sn is the three dimensional analog to stanene. Lastly, the Becke-Johson method is tested by calculating the electronic structure of bullk α-Sn and comparing several of the eigenvalues found to experiment.

3.1 Finding an Appropriate Pseudopotential and Exchange Correlation Functional

As discussed in Section 2.3, a pseudopotential is introduced to replace the difficult-to-solve problem of the core electrons and nucleii with a much smoother, easier to consider, effective

potential. This potential freezes out the core, leaving only the chemically active valence electrons to be explicity considered. A pseudopotential is created under the strict condition that the pseudo-orbital match the real orbital of an all-electron calculation after a set radius, known as r_{cut}. This study also requires that the effects of spin-orbit-coupling (SOC) be considered within this effective potential as the QSH effect arises directly from this interaction.

The open source, plane-wave pseudopotential code used for this study, ABINIT, possesses a library of pseudopotentials, but none consider the effects of SOC and so new pseudopotentials had to be constructed which do consider these effects. The Atomic Pseudopotentials Engine (APE) [59] package was then used to create pseudopotentials under the Troulier-Martins (TM) [60] scheme which use (i) the dirac wave equation, fully considering relativistic effects (labeled with *Dirac* or SO for "Spin-Orbit") and (ii) the scalar relativistic wave equation, which ignores the effects of SOC (labeled with *Scalar* or nSO for "non-Spin-Orbit"). These pseudopotentials were created by calculating the all-electron potential for a free neutral Sn atom using a modified Perdew-Burke-Ernzerhof (PBE) exchange-correlation potential, known as PBEsol [39], for both SO and nSO schemes. In addition to this, two pseudopotentials considering the SO and nSO schemes were created using the Becke-Johnson (BJ) [40] exchange-correlation potential. The pseudopotential utilizing the PBEsol exchange correlation was chosen as it has been shown to give better physical parameters (such as lattice constants) while the pseudopotential utilizing the BJ exchange correlation was chosen because it has been shown to obtain better eigenvalues when calculating electronic structure [36], [61].

To validate the pseudopotentials made using the APE, eigenvalues, ϵ_{ae}, of the valence orbitals of an excited state ($5s^1 5p^3$ for the scalar relativistic pseudopotentials and $5s^1_{\frac{1}{2}}\ 5p^1_{\frac{1}{2}}\ 5p^2_{\frac{3}{2}}$ for the fully relativistic pseudopotentials) using an all electron calculation should be compared with eigenvalues, ϵ_{psp}, calculated using the pseudopotentials (Table 3.1). Note here that the dirac pseudopotentials split the valence orbitals based on the *total* angular momentum j and the scalar pseudopotentials split the valence orbitals based on the *orbital* angular

Model	Orbital	r_{cut}	ϵ_{ae}	ϵ_{psp}
Scalar PBEsol	5s	2.283	-0.421	-0.423
	5p	2.483	-0.159	-0.160
	5d	3.975	0.0	0.0
Dirac PBEsol	$5s_{\frac{1}{2}}$	2.283	-0.421	-0.420
	$5p_{\frac{1}{2}}$	2.483	-0.172	-0.172
	$5p_{\frac{3}{2}}$	2.483	-0.154	-0.154
	$5d_{\frac{3}{2}}$	3.975	0.0	0.0
	$5d_{\frac{5}{2}}$	3.975	0.0	0.0
Scalar BJ	5s	2.283	-0.586	-0.575
	5p	2.483	-0.322	-0.319
	5d	3.975	-0.103	-0.104
Dirac BJ	$5s_{\frac{1}{2}}$	2.283	-0.580	-0.594
	$5p_{\frac{1}{2}}$	2.483	-0.330	-0.326
	$5p_{\frac{3}{2}}$	2.483	-0.313	-0.309
	$5d_{\frac{3}{2}}$	3.975	-0.096	-0.098
	$5d_{\frac{5}{2}}$	3.975	-0.096	-0.098

Table 3.1: Table of eigenvalues and cutoff radii for each pseudopotential scheme and valence orbital for a Sn atom. Note also that r_{cut} is in units of Bohr radii and the eigenvalues of each orbital for the all electron (ϵ_{ae}) and pseudopotential (ϵ_{psp}) are in units of Ha.

momentum l.

3.2 Convergence Study

When using a plane-wave pseudopotential code, there are two primary input parameters which determine the accuracy of a calculation's results: E_{cut}, the maximum plane-wave kinetic energy, and N_{kpt}, the finess of the k-space sampling grid, and, in order to yield consistent, accurate results, a convergence in total energy for each of these parameters is required. For the parameter E_{cut}, this is done by finding the system's total energy using varying values of E_{cut}, then plotting these values and determining where the change between two points is less than 0.001 Ha. The convergence criterion of 0.001 Ha was choosen to ensure the so-called "chemical accuracy" (that is, the accuracy required to make realistic chemical predictions). Figure 3.1 shows energy convergence for the typical diamond structure of α-Sn

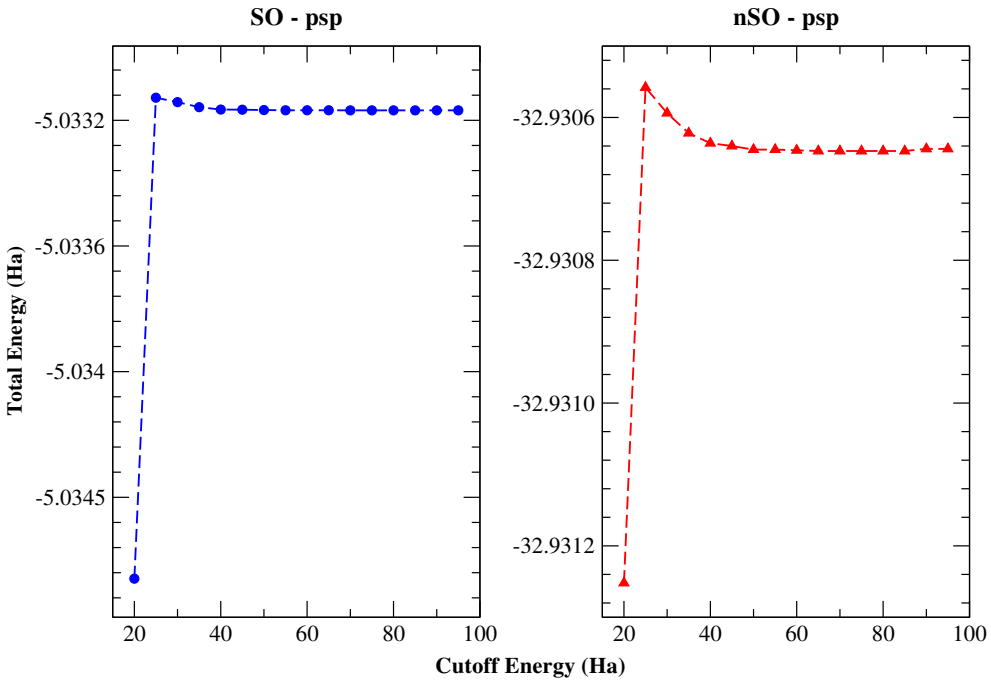

Figure 3.1: Total Energy is plotted against cutoff energy for (left) the fully relativistic pseudopotential (SO case) and (right) the scalar relavtivistic pseudopotential (nSO case).

past a cutoff energy of 40 Ha. This value of E_{cut} was then used as the cutoff energy for all further studies of tin and stanene for both the SO and nSO cases.

A second convergence study also had to be completed to determine a sufficient fineness of the k-space grid which also helps ensure a convergence, up to chemical accuracy, in total energy. The ABINIT documentation provides sample k-point grids which work well for simple geometries such as diamond or hexagonal lattices. For a lattice with fcc symmetry (i.e. a diamond structure), ABINIT suggests selecting the number of grid points along each of the three dimensions in reciprocal space and also provides several "shifted" k-point grids which enable an efficient sampling of k-space. Increasing the number of grid points increases the fineness of these shifted grids, and thus will increase the accuracy of the density. To test how fine a grid we needed, a similar convergence in total energy was done. The same convergence criterion ensuring chemical accuracy is used and a plot of total energy against the number of grid points along each direction in reciprocal space (N_{kpt}) is shown in Figure 3.2 which converges at $N_{kpt} = 10$ and will be used for the optimization and band structure calculations

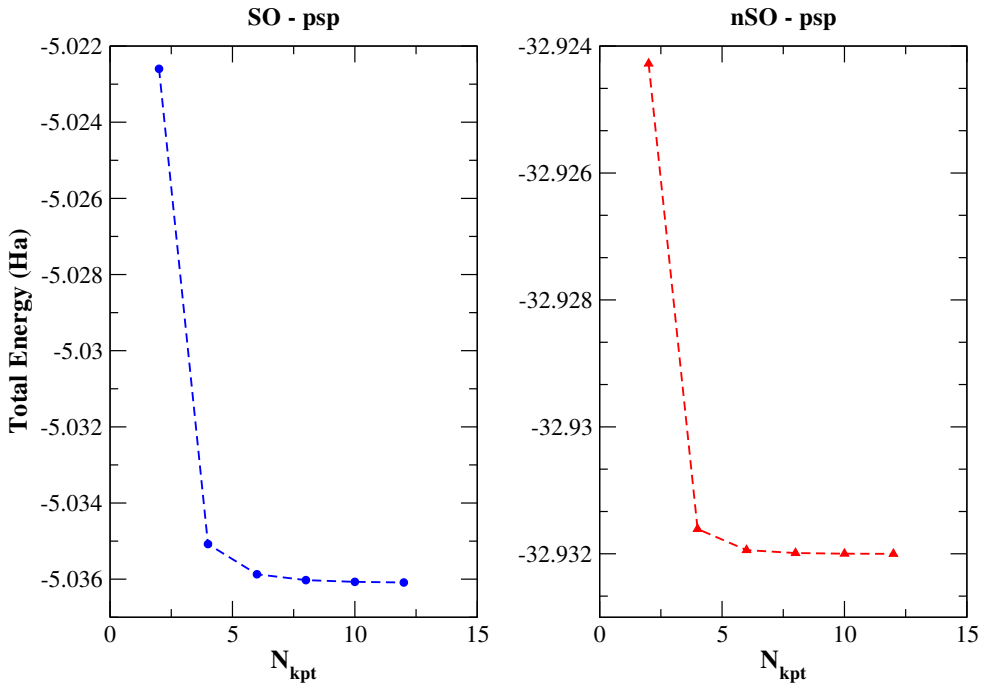

Figure 3.2: Total Energy is plotted against N_{kpt} for the SO (left) and nSO case (right).

of tin. When stanene is considered, a new k-point grid has to be defined more carefully and a detailed description of how this grid is constructed can be found in Section 4.1.2

3.3 Optimizing α-Sn Lattice

Bulk α-Sn is arranged in a conventional diamond structure akin to both silicon and germanium, a face centered cubic (fcc) lattice with a basis of two atoms at $a_0 \cdot (000)$ and $a_0 \cdot (\frac{1}{4}\frac{1}{4}\frac{1}{4})$ where a_0 is the lattice constant. The primitive translation vectors are:

$$\begin{aligned} \boldsymbol{a_1} &= \frac{a_0}{2}(\hat{\boldsymbol{x}} + \hat{\boldsymbol{y}}) \\ \boldsymbol{a_2} &= \frac{a_0}{2}(\hat{\boldsymbol{y}} + \hat{\boldsymbol{z}}) \\ \boldsymbol{a_3} &= \frac{a_0}{2}(\hat{\boldsymbol{z}} + \hat{\boldsymbol{x}}) \end{aligned} \tag{3.1}$$

and a schematic of the unit cell is shown in Figure 3.3.

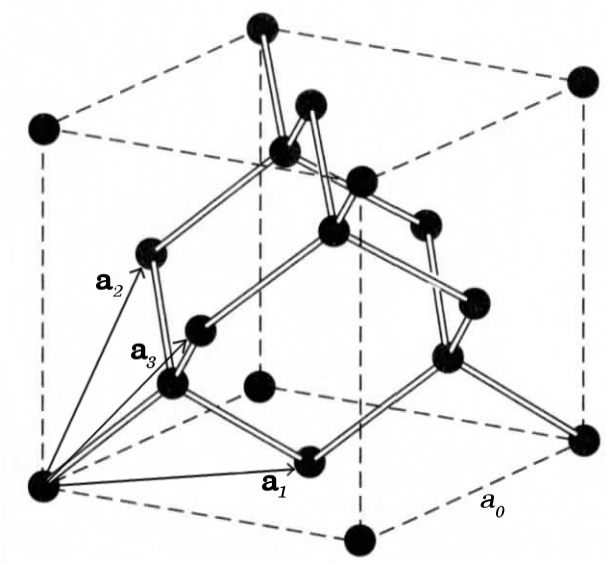

Figure 3.3: Diagram of the unit cell of the diamond structure. Primitive translation vectors are shown as $\boldsymbol{a_1}, \boldsymbol{a_2}$, and $\boldsymbol{a_3}$ with lattice constant, a_0. Note that a diamond structure has tetrahedral bonding characteristics, with 4 nearest neighbors and 12 next nearest neighbors.

Lattice constants were then found via a calculation of total energy with an increasing unit cell size (i.e. increasing lattice constant) using the spin-orbit (SO) and non-spin-orbit (nSO) pseudopotentials. For the SO case, the lattice constant was found to be 12.35 Bohr and for the nSO case a lattice constant of 12.31 Bohr was found and a plot of this study can be found in Figure 3.4. These values are 0.7% and 0.3% larger than the experimental lattice constant (6.488 Å) respectively. Cohesive energies for the SO and nSO pseudopotential were also found via a calculation of total energy for an isolated tin atom and subtracting it from the total energy per atom in the diamond structure of tin. These energies were found to be 0.132 Ha and for the nSO case and 0.156 Ha for the SO case. These values are 14.3% and 34.1% larger than experimental measurements and a table containing these values along can be found in Table. 3.2.

A previous graduate student, Zach Nault, studied the accuracy of using the PBEsol exchange potential to calculate lattice constants and cohesive energies for several different metals, semiconductors, transition metals, and ionic compounds [45]. Unfortunately, he did not consider tin in his study, but did conduct studies on carbon, silicon, and germanium

	PBEsol	Exp.
Lattice Constant(Å):		
SO	6.535	6.488
nSO	6.514	6.488
Cohesive Energy(eV):		
SO	4.211	3.14
nSO	3.591	3.14

Table 3.2: Table of lattice constants and cohesive energies calculated using the PBEsol exchange functional compared with experimental values found in [5].

which are chemically similar. In this study, it was found that the PBEsol functional finds lattice constants within 1% of experimental values for C and Si and finds a Ge lattice constant within $\sim 1.5\%$ of experiment. Cohesive energies were also found to be within $\sim 9\%$, $\sim 7\%$, and $\sim 2\%$ of experiment for C, Si, and Ge respectively.

Overall, for obtaining lattice constants, the PBEsol functional does well in agreeing with experiment for both the SO and nSO schemes. Percent error for cohesive energies, however, remains fairly large, even when compared to [45], but since this study is focused primarily on structural properties, the PBEsol functional will work well for the purposes of this thesis. It should also be noted that utilizing the fully relativistic wave equation (the SO scheme) does not significantly improve calculations of structural properties and in fact, the scalar relativistic wave equation (the nSO scheme) calculates structural properties more accurately for Sn.

3.4 Calculating α-Sn Band Structure and Comparing to Experiment

Band structures were also found for both the SO and nSO cases (Figure 3.6). To do this, we solve the Kohn-Sham equation for many different k points, along a path of high symmetry lines of the diamond Brillouin zone, $L \to \Gamma \to X \to \Gamma'$ (where Γ' is the center of the next

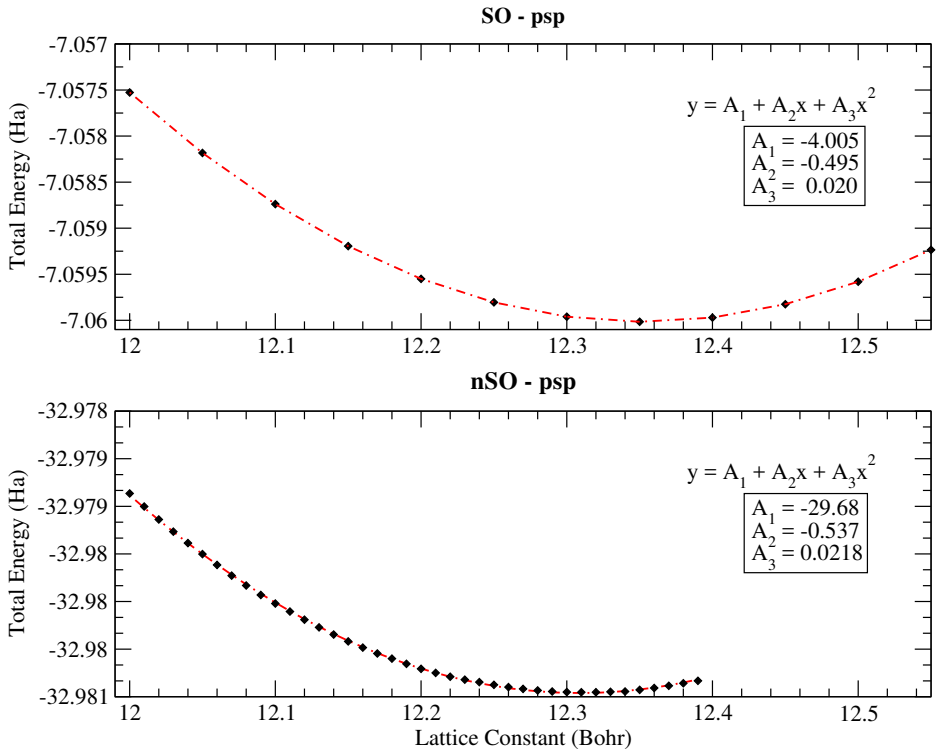

Figure 3.4: Convergence of lattice constant for the fully relativistic pseudopotential (top) and the scalar relativistic pseudopotential.

cell along the (111) direction), and plots the eigenvalue against each k point. For the SO case, the bands separate states based on the momentum vector, k, which is coupled with the spin direction, m_s, while for the nSO case, the bands separate states based only on the momentum vector k (hence spin direction is not considered, making the bands degenerate). The bands split for the SO case because the corresponding pseudopotential considers the total angular momentum j of a state rather than just the orbital angular momentum l. The nSO pseudopotential does not consider the spin of an electron to influence the energy of the state and so only the orbital angular momentum is considered.

A closer look at Fig. 3.6 reveals that there are 4 occupied valence bands (as there are 8 atoms per unit cell) and 4 unoccupied conduction bands which are indicated in blue and red respectively. For the nSO case, the topmost valence band is doubly degenerate and splits up into two bands when spin-orbit coupling is considered. These valence bands, when examined at the Γ point, can be considered as the traditional valence orbitals of a freestanding Sn

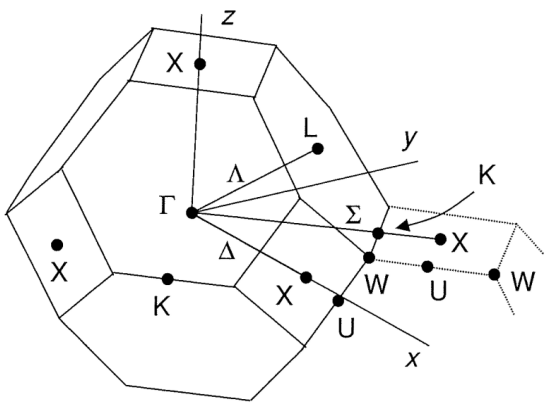

Figure 3.5: Brillouin Zone of an fcc lattice with important points labeled. Figure taken from [3].

atom. The bottomost valence band is an s-like state while the topmost three valence bands are p-like. The splitting that occurs for the two highest valence bands at the Γ point can be attributed to a p-like state that splits into separate $j = \frac{3}{2}$ and $j = \frac{1}{2}$ states. In addition to this, the second conduction band is also doubly degenerate and splits into two conduction bands in the SO scheme. These results indicate that the spin-orbit coupling interaction is being considered correctly in our calculations and a determination of its effects on stanene can be investigated.

It was shown in the previous chapter that the Becke-Johnson method obtains more accurate eigenvalues. Utilizing this correction provides a more realistic band structure for bulk α-Sn, obtaining much more accurate eigenvalues at the L and Γ point (Table 3.3). Figure 3.7(b) demonstrates that the PBEsol functional calculates bulk α-Sn to be metallic and not semiconducting (evidenced by the lowest conduction band reaching below the fermi energy). In addition, many of the eigenvalues at the L and Γ points in the band structure possess an average percent error of $> 50\%$ when compared to experiment. The Becke-Johnson functional, however, provides significantly more accurate eigenvalues, with an average percent error of 13.5% for the points listed in Table 3.3, the locations of which are shown in Figure 3.7(a).

It should be noted however, that when investigating structural properties, the PBEsol

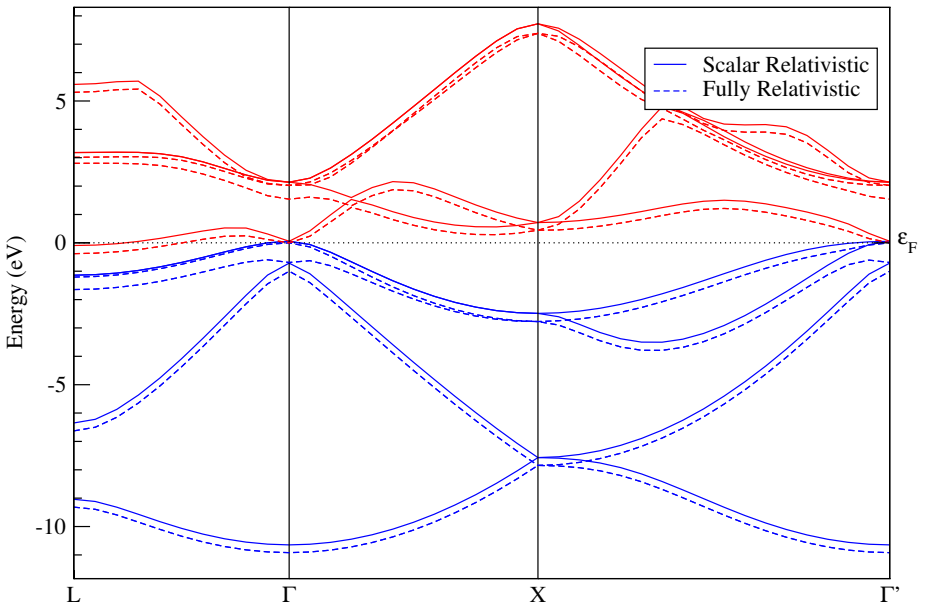

Figure 3.6: Band structure for scalar relativistic (solid lines) and fully relativistic (dashed lines) pseudopotential. Notice that once spin-orbit coupling is considered, the degeneracy is broken in several bands at the Γ point.

Energy (eV)	PBEsol	BJ	Exp.
Γ_{7v}	-1.002	-0.67	-0.8
Γ_{7c}	-0.692	-0.591	-0.634
L_{6c}	-0.381	0.066	0.09
Γ_{6c}	1.540	1.87	1.98

Table 3.3: Table comparing eigenvalues (measured with respect to the fermi energy) of several bands at the L and Γ point calculated using the PBEsol and BJ functionals to experiment [4].

functional remains supreme. Thus, this thesis will utilize a marriage between the PBEsol and Becke-Johnson functionals. The PBEsol functional will be used for structural investigations, and the Becke-Johnson functional will be utilized for electronic structure calculations.

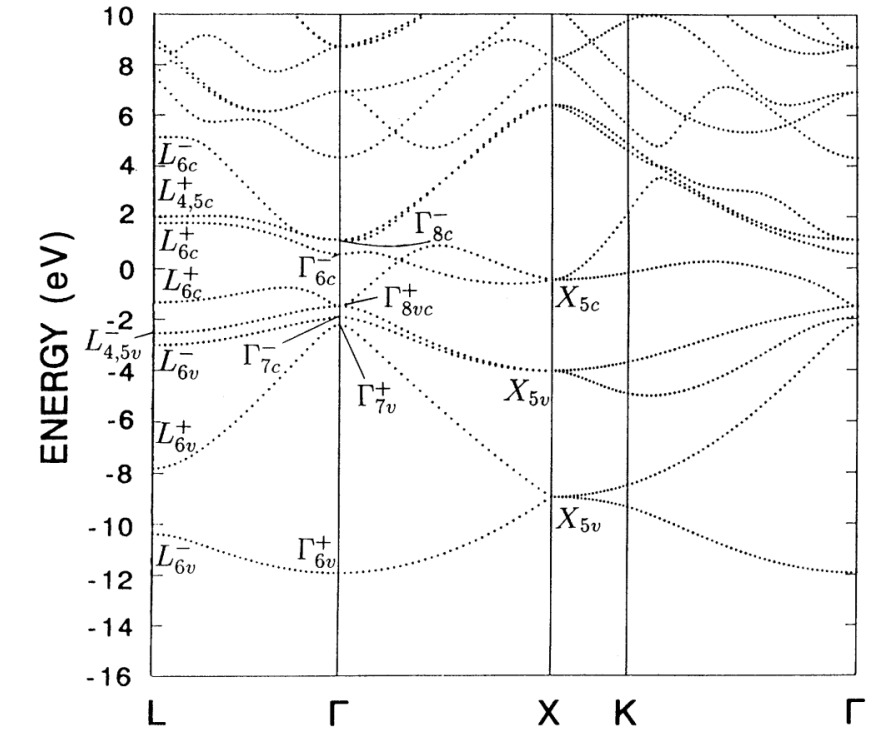

(a)

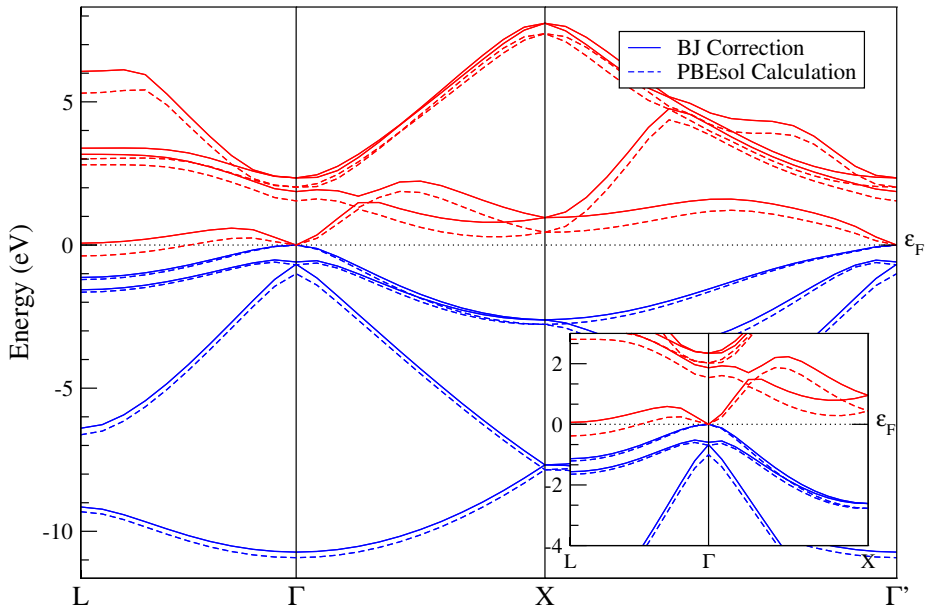

(b)

Figure 3.7: Band structure for α-Sn published by *Argonne National Laboratory* [4] (a). Band structure of α-Sn comparing the PBEsol exchange correlation with that of the Becke-Johnson correction with an inset depicting the improvement of energy at the L point (b).

Chapter 4

Analysis of Monolayer Tin

This chapter discusses the characterization of monolayer tin (known as stanene) and investigates its electronic properties. The characterization of stanene, shown in section 4.1, is achieved by shaving a single layer of bulk α-Sn along the (111) direction, converging a vacuum layer (so as to kill any mirror layer interactions), and choosing a sufficient k-point grid. Following this, an optimzation of the unit cell (lattice constant) and basis atom positions is executed. After the characterization of the system, electronic structure, band gap energies, and densities of states are found for the monolayer along with a brief discussion about the similarities in electronic behavior to graphene and other Group IV monolayer materials.

4.1 Characterizing Stanene

4.1.1 Creating a Lattice and Converging a Vacuum Layer

Since the primitive translation vectors of a fcc lattice (shown in Figure 4.1) are separated by an angle of 120° when viewed along the body diagonal, α-Sn possesses hexagonal symmetry. Because of this, stanene can be built by shaving off a single layer of the diamond structure along the (111) direction. To do this, the primitive translation vectors of a face-centered cubic lattice, $\boldsymbol{a_1} = a_0 \cdot (\frac{1}{2}\ \frac{1}{2}\ 0) = \boldsymbol{a_1'}$ and $\boldsymbol{a_2} = a_0 \cdot (\frac{1}{2}\ 0\ \frac{1}{2}) = \boldsymbol{a_2'}$, are used to find a third

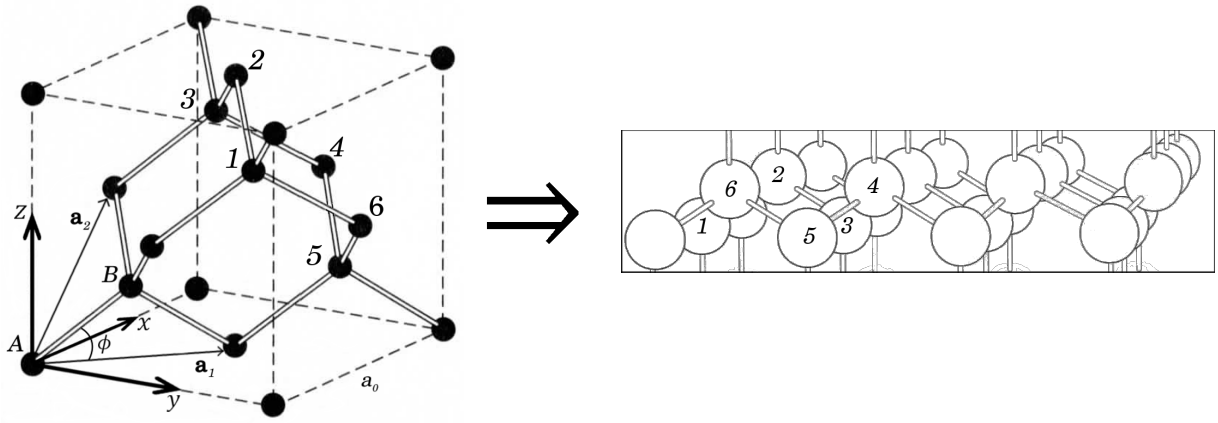

Figure 4.1: Diagram of a diamond crystal. Primitive translation vectors $\boldsymbol{a_1}$ and $\boldsymbol{a_2}$ are shown along with the basis atoms A and B, lattice constant a_0, and buckling angle ϕ. Original figure taken from [5].

translation vector that is perpendicular to both and also points to the next layer of Sn atoms, $\boldsymbol{a_3'} = \frac{\boldsymbol{a_2}\times\boldsymbol{a_1}}{\frac{a_0}{4}} = a_0\frac{n}{3}\cdot(-111)$ (here n is the number of "layers" before arriving at the next unit cell). The diamond structure also classically has a basis of two atoms at coordinates $a_0\cdot(000)$ and $a_0\cdot(\frac{1}{4}\frac{1}{4}\frac{1}{4})$ within the reduced coordinate system (a system wherein a coordinate, $(n'm'l')$, corresponds to a real space location of $\boldsymbol{r} = n'\boldsymbol{a_1} + m'\boldsymbol{a_2} + l'\boldsymbol{a_3}$). This requires that our new system position the first atom at the origin and the second atom at $(\frac{1}{3}\ \frac{1}{3}\ \frac{1}{4n})$ which coresponds to a location of $\boldsymbol{\tau_2'} = \frac{1}{3}\boldsymbol{a_1'} + \frac{1}{3}\boldsymbol{a_2'} + \frac{1}{4n}\boldsymbol{a_3'}$) to ensure the second basis atom remains in its classical location of $a_0\cdot(\frac{1}{4}\frac{1}{4}\frac{1}{4})$.

To ensure that a single layer of tin was isolated, $\boldsymbol{a_3'}$ needed to be increased until the total energy was again converged to a millihartree. In this system, each successive layer of Sn atoms lies at $a_0\cdot(-\frac{1}{3}\frac{1}{3}\frac{1}{3})$ and so to remove any mirror interactions, each component of the translation vector $\boldsymbol{a_3}$ was increased by $\frac{1}{3}$ until the total energy had converged. The results of this study are shown in Figure 4.2 with the converged translation vector being $\boldsymbol{a_3} = a_0(-\frac{4}{3}\frac{4}{3}\frac{4}{3})$.

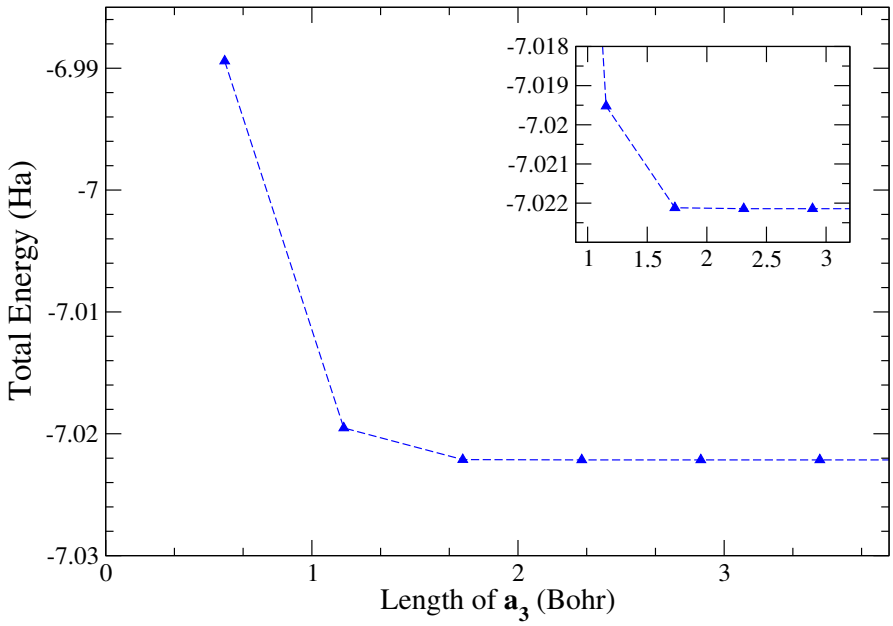

Figure 4.2: Vacuum convergence study, total energy is plotted against $|\boldsymbol{a_3}|$ for the SO pseudopotential.

4.1.2 Finding a K-Point Grid

Once the lattice vectors and basis were found, a minimized grid of k-points which efficiently sample the Brillouin zone was obtained using the method of Monkhorst and Pack [62]. The ABINIT documentation provides sample k-point grids which work well for simple geometries such as diamond or hexagonal lattices, but, since the geometry of the system is a bit more complex, a unique grid has to be found. Luckily, by default, if a k-point grid is not defined, ABINIT will automatically generate a set of possible k-point grids. The grids that are chosen can then be printed out alongside a figure of merit, which measures the efficiency of each grid. The fineness of these reciprocal space grids is determined by a cutoff wavelength, which corresponds to the maximal wavelength of a plane wave. This maximal wavelength should span across a supercell, made of many unit cells in real space and equates to a minimum length in reciprocal space. Thus, having a large cutoff wavelength corresponds to a small value of k and therefore a finer grid (see Figure 4.3). These grids are expressed as a super-lattice in real space, defined as:

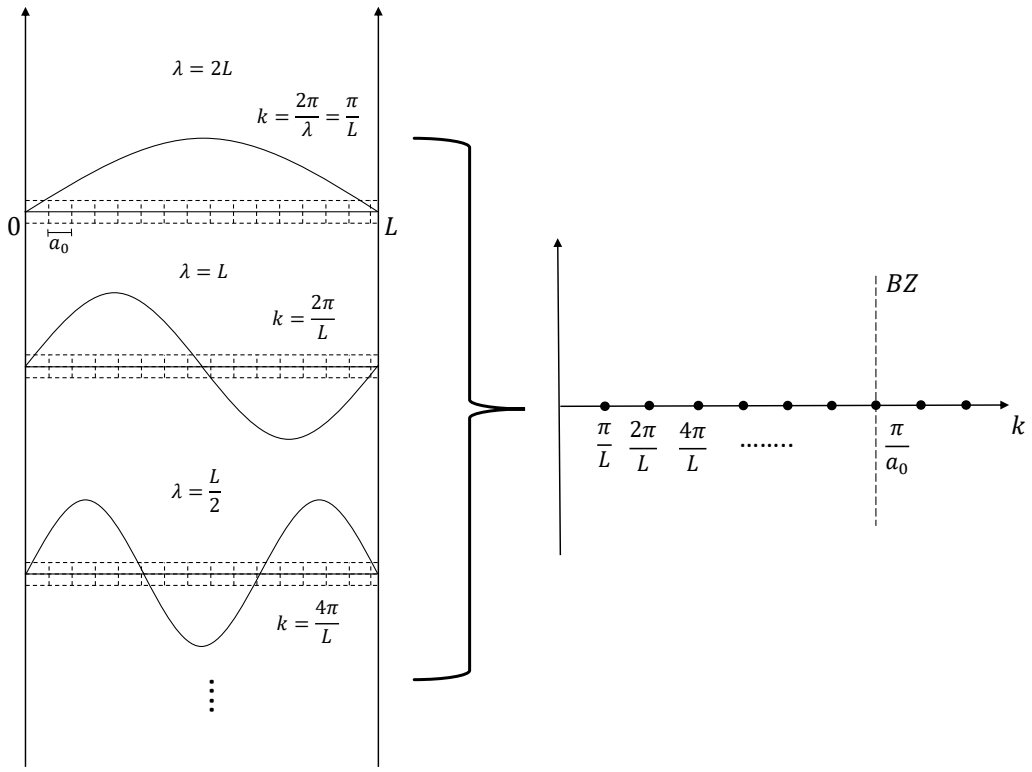

Figure 4.3: Schematic of several plane waves moving through a supercell of length $L >> a_0$ (left) and the resulting one-dimensional grid of points in k space (right). The input parameter *kptrlen* in equivalent to $2L$ in this diagram, demonstrating the relationship between this real space length, and the fineness of the k-point lattice.

$$\begin{aligned} \boldsymbol{a_1'} &= k_{11}\boldsymbol{a_1} + k_{12}\boldsymbol{a_2} + k_{13}\boldsymbol{a_3} \\ \boldsymbol{a_2'} &= k_{21}\boldsymbol{a_1} + k_{22}\boldsymbol{a_2} + k_{23}\boldsymbol{a_3} \\ \boldsymbol{a_3'} &= k_{31}\boldsymbol{a_1} + k_{32}\boldsymbol{a_2} + k_{33}\boldsymbol{a_3} \end{aligned} \tag{4.1}$$

(where k_{ij} is an integer and is expressed within a matrix), the reciprocal of which is the k-point lattice. An initial matrix was chosen and a convergence study in total energy was done by increasing the size of each component within this chosen matrix, yielding a final

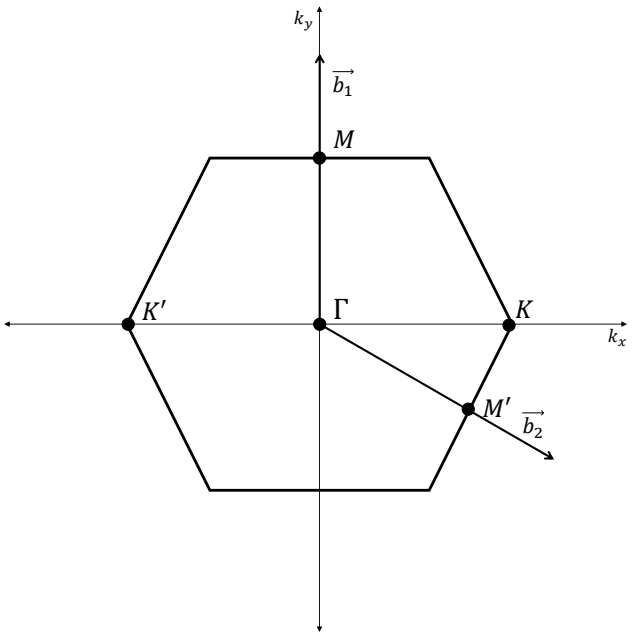

Figure 4.4: Two dimensional hexagonal Brillouin zone which shows the reciprocal lattice vectors, $\boldsymbol{b}_1$ and $\boldsymbol{b}_2$ along with the high symmetry points, M, Γ,and K.

grid of:

$$\begin{pmatrix} 11 & 0 & 0 \\ -11 & 11 & 0 \\ 0 & 0 & 1 \end{pmatrix}. \tag{4.2}$$

Armed with this matrix, we now have enough information to map out the k-space we will be exploring; the two-dimensional Brillouin Zone (Figure 4.4).

4.1.3 Cell Optimization

Following the vacuum and k-point grid convergence study, an optimization of the volume of the cell and the position of the basis atoms needed to be done. A modified Broyden-Fletcher-Goldfarb-Shanno (BFGS) minimization, which takes into account the gradients of the total energy, along with total energy itself [63], was used to perform this. The algorithm was set to optimize only the volume of the unit cell and atom positions, and the converged cell size, a_0, was found to be 12.251 Bohr and the position of the atoms were found to be

$(0, 0, 0.003)$ and $(\frac{1}{3}, \frac{1}{3}, 0.0596)$ in the reduced coordinate system. The optimization shrinks the lattice constant, a_0, slightly ($\sim 8\%$) along with the bond length between basis atoms ($\boldsymbol{r}_{Sn} = 5.34$ Bohr and $\boldsymbol{r}_{Stan} = 5.19$ Bohr). The buckling angle (discussed in Section 5.1), ϕ, decreases slightly as well ($\phi_{Sn} = 35.26°$ and $\phi_{Stan} = 34.8°$).

4.2 Electronic Structure and Density of States

Once stanene had been characterized, the electronic structure was calculated for the SO and nSO pseudopotential by solving the Kohn-Sham equation along along the high symmetry path, $M \to \Gamma \to K \to M'$. In Figure 4.5 we see four valence bands (shown in blue) which each hold two electrons. Additionally, the parity of each valence band at the TRIM points is shown. At the K point, there is a linear crossing of the highest occupied and lowest unoccupied bands for the nSO pseudopotential, but for the SO pseudopotential, a gap of 83.5 meV is induced. The inset in Fig. 4.5 shows this gap in more detail. This feature can be seen in most Group IV monolayer materials [64] and opens explicitly because of the effects of spin-orbit coupling, a fundamentally different reason than for typical semiconductors, indicative of a QSH insulating phase.

This linear band crossing at the K point in the 2D hexagonal BZ (Figure 4.4) between the highest occupied and lowest unoccupied molecular orbital (HOMO and LUMO respectively) can also be found in graphene [65]. These states are known as dirac cones and can be modeled as massless fermionic quasiparticles moving at an effective "local" speed of light, v_f. These quasiparticles follow the same behavior as a relativistic fermion with energy:

$$E = \pm\sqrt{p^2 v_F^2 + \Delta_{SO}^2}\,, \tag{4.3}$$

where Δ_{SO} is a parameter equal to $\frac{1}{2}E_{Gap}$, and is a measure of the strength of the spin-orbit interaction. This term can also be related to an effective mass, m_*, which the modeled fermion possesses. To find these values we fit the nSO band structure to pull out v_f then fit

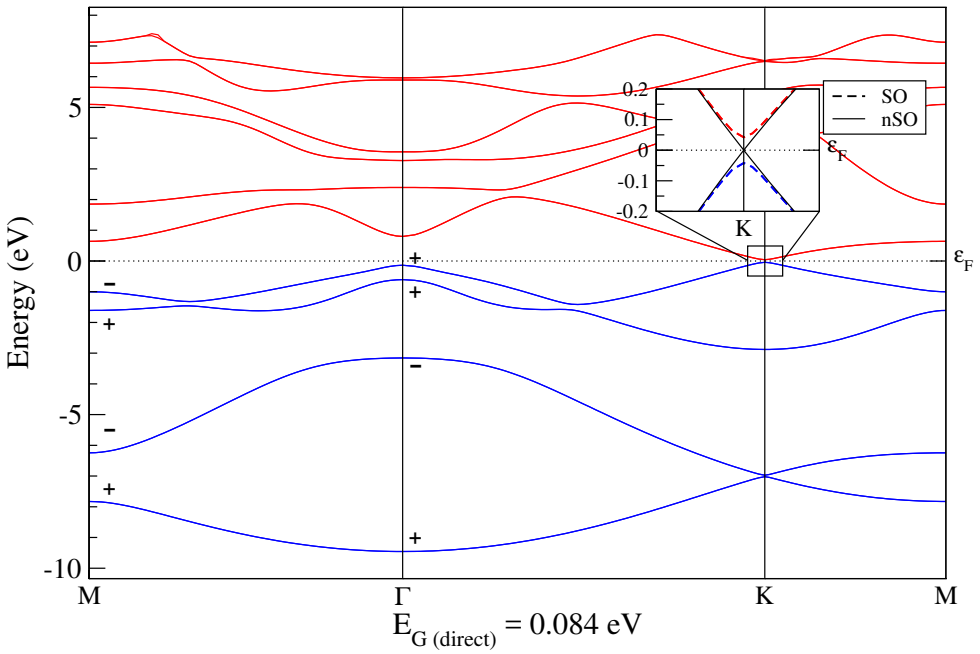

Figure 4.5: Electronic structure of Stanene monolayer using the SO and nSO (inset) pseudopotential. Note that there was a numerical error in the calculation of the fermi energy, misplacing the eigenvalues of each band by $\approx 0.015\ eV$. To account for this, each band from the SO pseudopotential calculation was shifted up by $0.0155\ eV$ in order to center the gap around the fermi energy.

the SO band structure to find Δ_{SO}, keeping the previous v_f. The results from fitting these bands found $v_F \approx 19 * 10^7 ms^{-1}$ and $\Delta_{SO} = 0.0418\ eV$ (shown in Figure 4.6).

Further verification of a topologically nontrivial state can be found through the use of a "parity trick" to calculate the Z_2 invariant, ν, in 2D systems [53]. This involves determining the parity of the Bloch wave functions at the TRIM points, Γ and M, for each valence band. If the net parity is negative, $\nu = 1$ and a topologically nontrivial state is present while if the net parity is positive, $\nu = 0$ and the system is topologically trivial. Parity at these two points was determined by visualizing the density for each valence band using the Visual Molecular Dynamics (VMD) software package [6] (Fig. 4.7 and 4.8). A center of inversion symmetry was chosen in the unit cell and the presence of a bonding or antibonding state determined the parity (positive and negative respectively).

Following this, the density of states (DOS), essentially a histogram of the number of orbitals per unit energy, was calculated. The density of states is a useful tool for analyzing

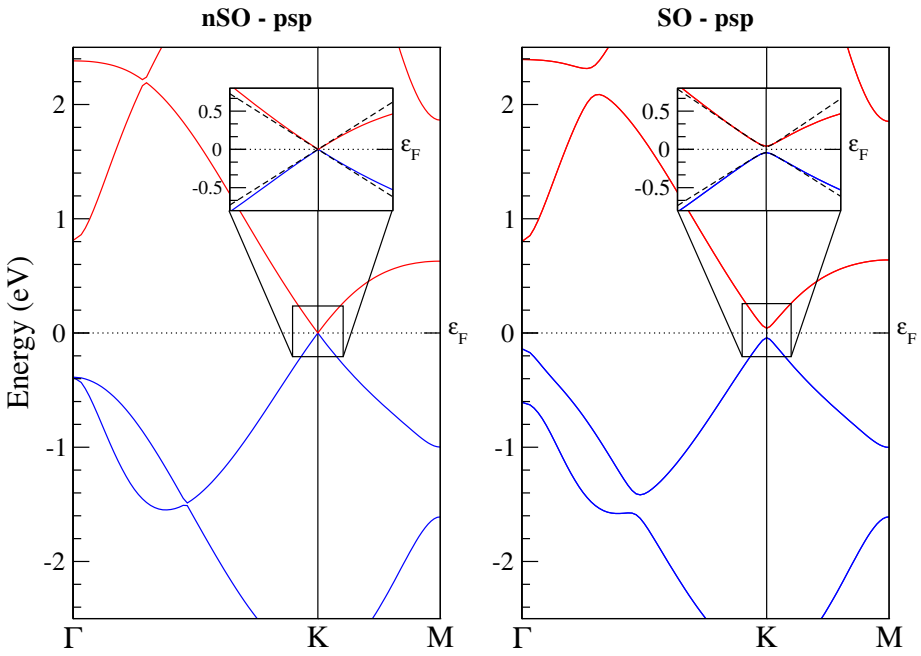

Figure 4.6: Band structure for SO and nSO pseudopotential. The results of the linear regression are shown in the inset of the nSO-psp plot (left) while the results from fitting Eq. 4.3 are shown in the inset of the SO-psp plot (right).

the electronic structure of solids which also provides a more accurate fermi energy. To perform this calculation, a higher density k-point grid is required because the resolution of the density of states is much more sensitive to the number of k-points than a typical band structure. To calculate the density of states, the magnitude of each index within the k-point grid was tripled, yielding a matrix of:

$$\begin{pmatrix} 33 & 0 & 0 \\ -33 & 33 & 0 \\ 0 & 0 & 3 \end{pmatrix}, \tag{4.4}$$

(the results of which are shown in Fig. 4.9). The calculation also provided a fermi energy of $E_f = -4.001\text{eV}$ and Figure 4.9 demonstrates the small band gap at the K point in the Brillouin zone.

The DOS demonstrates that the gap at the K point is a true gap throughout *all* reciprocal space. Also, the features in the DOS plot at $\sim -7\ eV$ should be seen at the

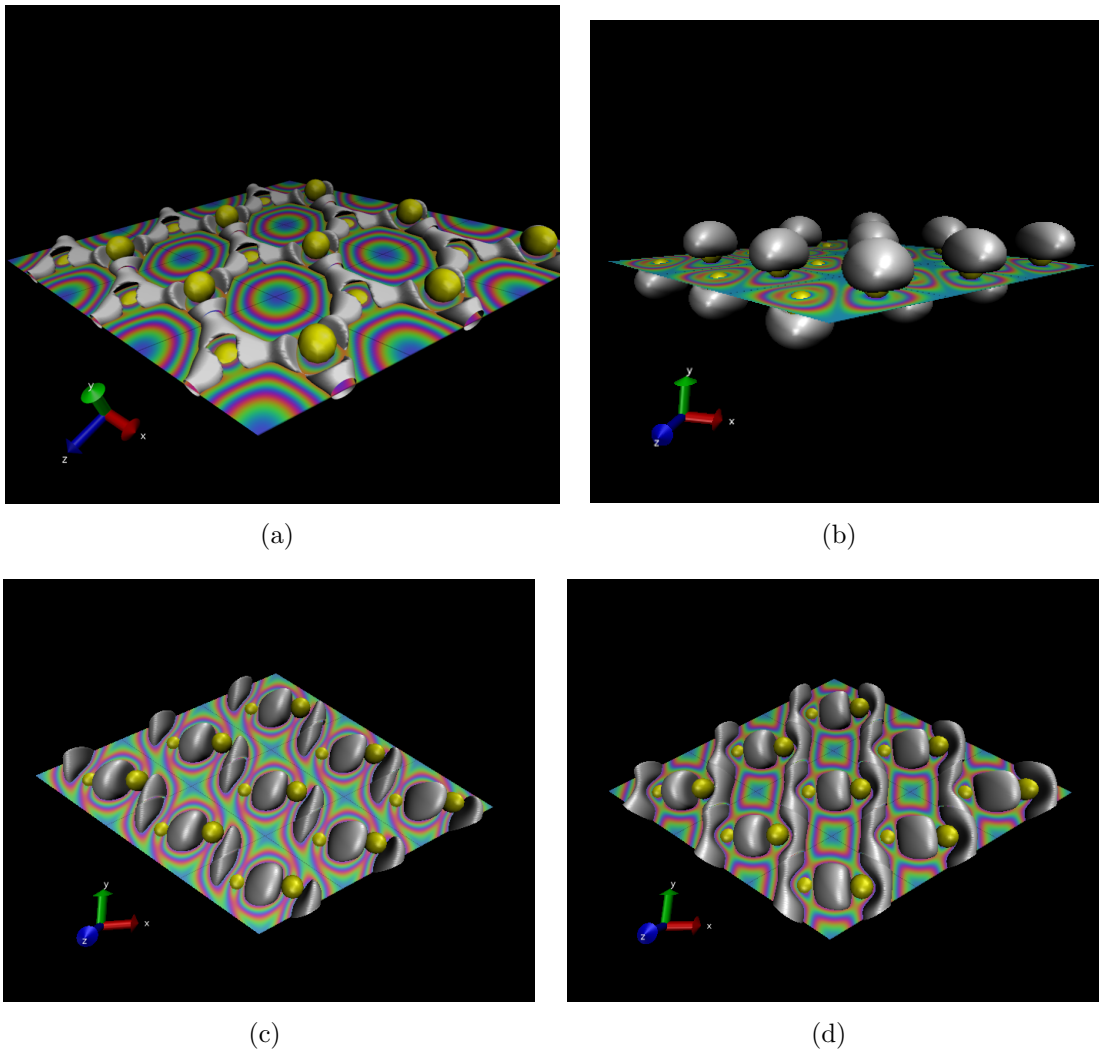

(a) (b)

(c) (d)

Figure 4.7: Visualization of the density (gray) at the Γ point for the first (a), second (b), third (c), and fourth (d) valence band. All states, save for (b) were determined to have positive parity.

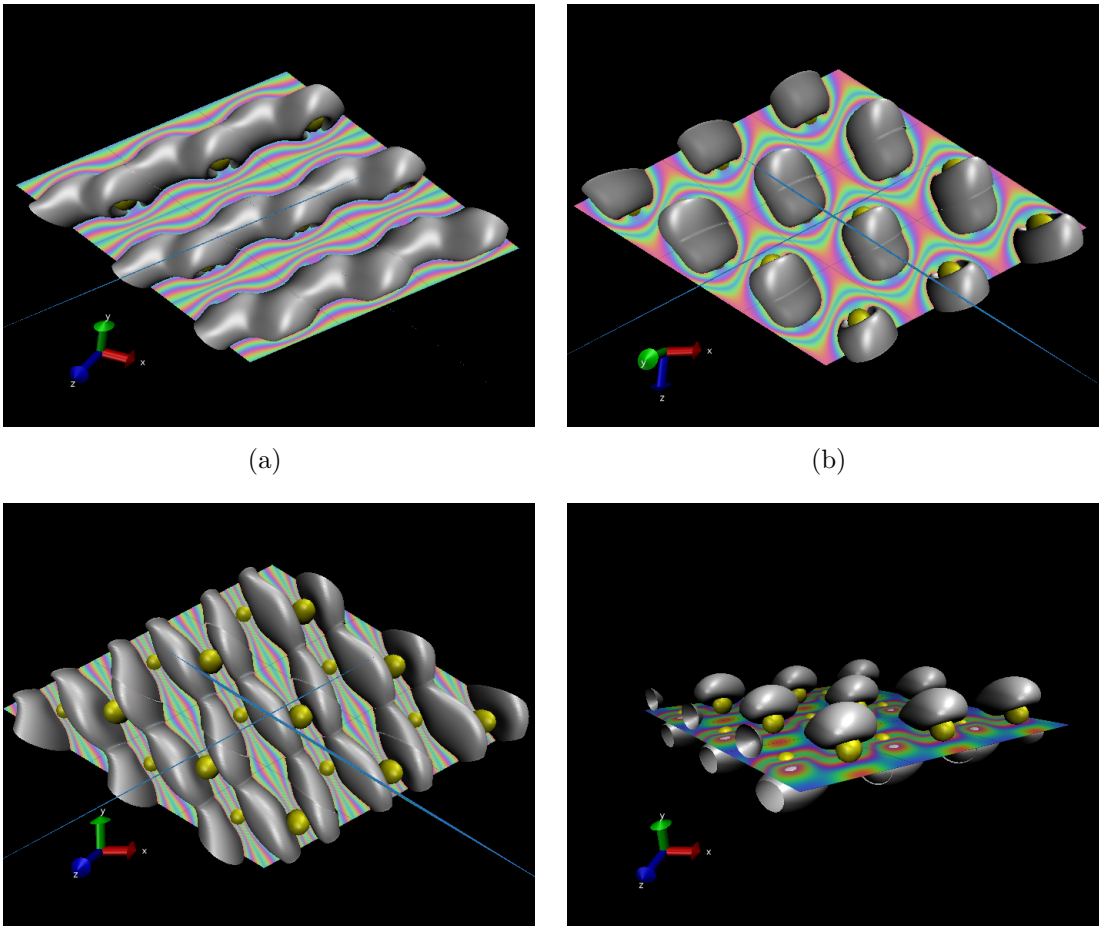

(a) (b)

(c) (d)

Figure 4.8: Visualization of the density (gray) at the M point for the first (a), second (b), third (c), and fourth (d) valence band. State (a) and (c) were determined to have positive parity while (b) and (d) were determined to have negative parity.

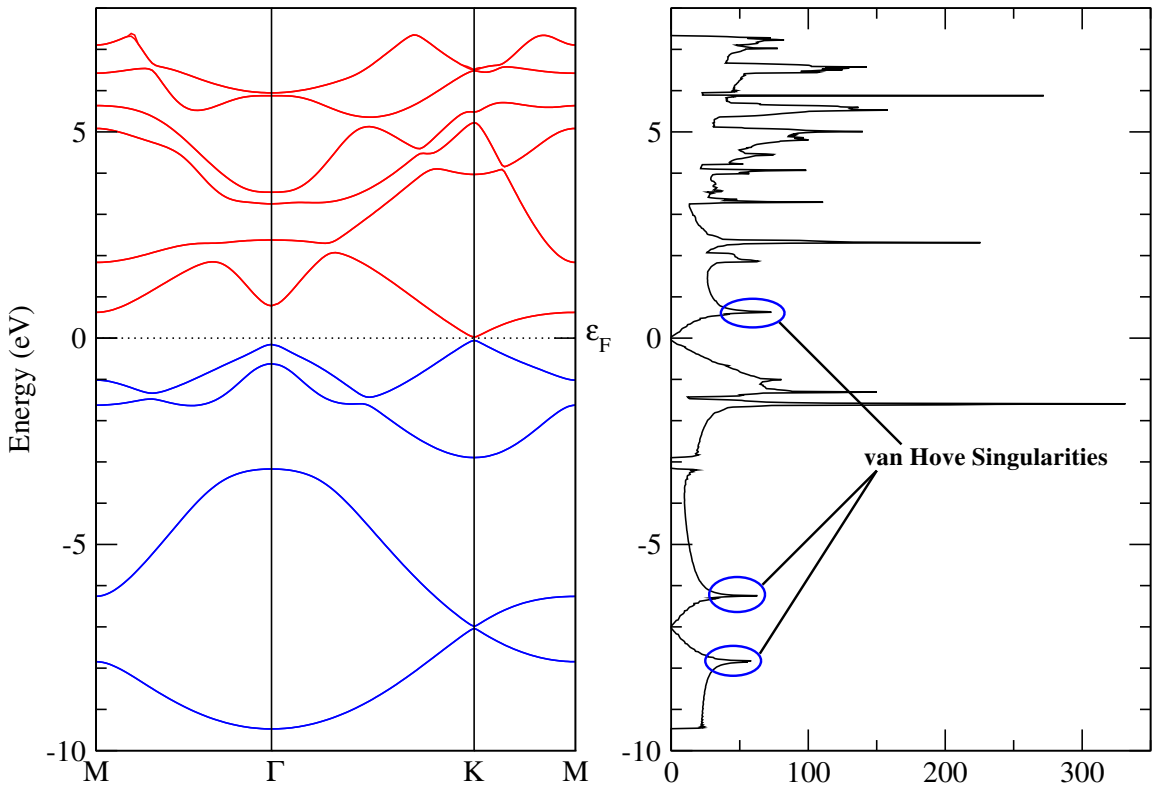

Figure 4.9: Band structure of monolayer stanene (left) and the corresponding density of states (right).

fermi level were it not for the features near the gamma point polluting the density of states. These "spikes" in density are known as van Hove singularities which are also found in doped and twisted bilayer graphene [66], [67]. In addition, it is importrant to note that the DOS near the fermi energy does not drop immediately near the gap like classical gaps. Instead, it decreases linearly both near the fermi energy and at $-7\ eV$.

Chapter 5

Investigating The Structural Properties of Stanene

In chapter 4, the structural properties of stanene were found and an analysis of its electronic structure exploring the band gap, confirming its topological characteristics, and calculating densities of states were all discussed. This chapter explores the structural stability of monolayer and multilayer stanene through compressive biaxial strain. This is followed by a discussion of the structural properties of these configurations including the buckling between basis atoms as well as unique structures that appear for the trilayer. Lastly, the electronic properties of multilayer stanene are explored and the merits of the Becke-Johnson method are discussed.

5.1 High-Buckled and Low-Buckled Phase of Stanene

The buckled, graphene-like configuration of stanene is characterized by a low buckling angle between the two basis atoms and will be refered to here as the low-buckled (LB) phase. The globally stable configuration, however, has a much larger buckling angle and, optimally, is a hexagonal close packed (HCP) bilayer. This configuration will be referred to as the high-buckled (HB) phase. A visualization of both the HB and LB phases of stanene along with

the buckling parameter and buckling height are also shown in Fig. 5.1.

To verify the results from [29], stability was explored for a monolayer of tin by simulating biaxial compressive strain through varying the magnitude of the primitive translation vectors, $\boldsymbol{a_1}$ and $\boldsymbol{a_2}$, from 110% of $\boldsymbol{a_1}$ and $\boldsymbol{a_2}$ to 80% of $\boldsymbol{a_1}$ and $\boldsymbol{a_2}$. At each step, a BFGS minimization was done to find optimized atom positions within the unit cell. Following this, total energy per atom at each of these optimized positions was calculated and a 2D lattice constant parameter for each strain value was then defined as:

$$a_{2D} = \sqrt{a_{1,x}^2 + a_{1,y}^2} \tag{5.1}$$

(the results of which are shown in Figure 5.2).

In addition, a buckling parameter, Δz, was also calculated. This parameter was defined as the distance between the two atom basis along the $\hat{z}$ direction and a plot of Δz against a_{2D} shown in Figure 5.3 shows a sharp transition from the LB to the HB phase for the monolayer as the lattice is compressed. Electronic structure was also calculated for the HB phase and demonstrates (Figure 5.9) that this configuration is metallic, killing the QSH insulating phase.

This strain study demonstrates that there are two locally stable phases of stanene: the low-buckled phase (LB) and the high-buckled phase (HB), but that the HB phase is the global energy minimum. This then brings up the primary question of this chapter: how do we ensure the low-buckled phase remains the most stable state?

5.2 Exploring Multiple Layers

In the bulk, tin is stable in two phases: α-Sn, which is a semiconductor arranged in a diamond structure, and β-Sn, which is metallic and arranged in a simple cubic lattice. In nature, the semiconducting phase, α-Sn, is more stable at low temperatures ($\sim$ -30°C). In a phenomenon known as "tin pest", a sample of the metallic, β, phase of tin will spontaneously

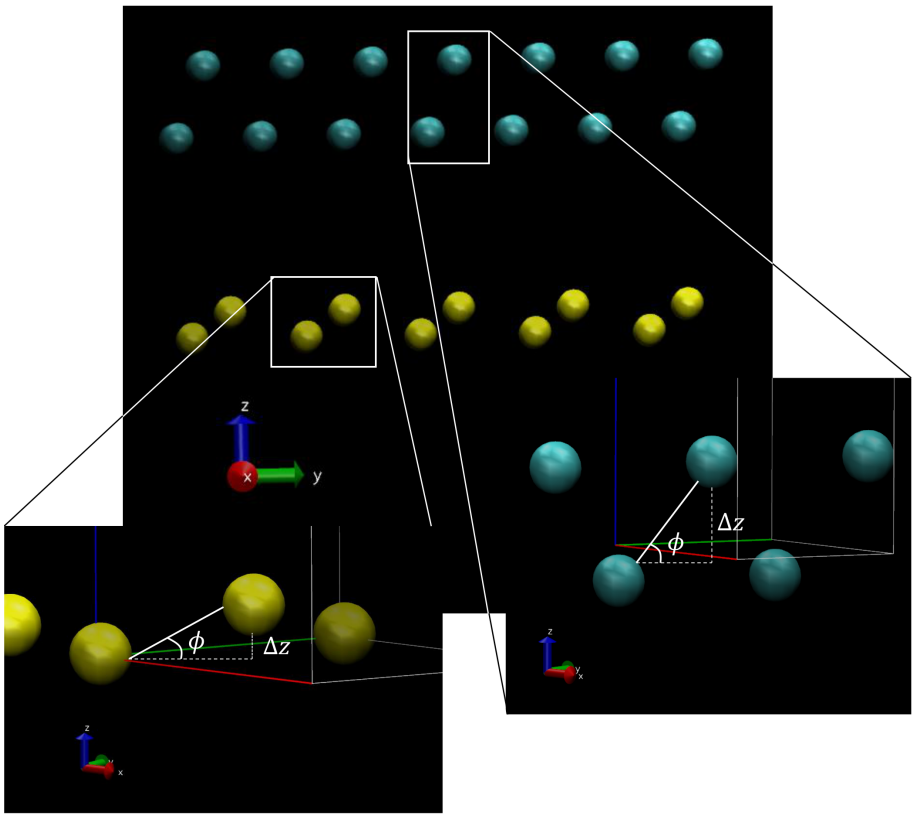

Figure 5.1: Image of High-Buckled (cyan) and Low-Buckled (yellow) stanene demonstrating the buckling angle, ϕ, and buckling height, Δz. (Images created using the Visual Molecular Dynamics [VMD] software package)

transition to α-Sn at sufficiently low temperatures. It would seem likely, then, that, since the LB configuration is derived from α-Sn, somewhere between the monolayer and bulk phases of tin, the LB configuration would become the globally stable state. To test this, a second and third layer of stanene was introduced and a strain study, described in Section 5.1, was done on the two materials as a method of stablizing stanene. The buckling parameter, Δz, was also calculated for these configurations and the results can be seen in Fig. 5.2 and 5.3.

A second layer of stanene is introduced by placing two additional basis atoms within the unit cell: one directly above the 2nd atom within the first basis at $(\frac{1}{3}\frac{1}{3}\frac{1}{5})$, and the other at $(\frac{2}{3}\frac{2}{3}$ 0.262) in the reduced coordinate system. To ensure the vacuum layer remains converged, the translation vector $\boldsymbol{a_3}$ was also increased to $\boldsymbol{a_3}$=$a_0(-\frac{5}{3}\frac{5}{3}\frac{5}{3})$. An optimization of atom positions was then done using the BFGS algorithm which found optimized positions

of: $\boldsymbol{\tau_1}$ = (0 0 0.003), $\boldsymbol{\tau_2}$ = ($\frac{1}{3}\frac{1}{3}$ 0.052), $\boldsymbol{\tau_3}$ = ($\frac{1}{3}\frac{1}{3}$ 0.209), and $\boldsymbol{\tau_4}$ = ($\frac{2}{3}\frac{2}{3}$ 0.258) in the reduced coordinate system. The average bond length between intralayer atoms was found to be $\boldsymbol{r_{intra}}$ = 5.26 Bohr and the average buckling angle was $\phi = 35.29°$. The interlayer bond length was found to be $\boldsymbol{r_{inter}} = 6.64$ Bohr. The bilayer was then strained in the same way as the monolayer which finds that the high-buckled phase remains more stable, but that the difference in energy between the HB and LB phase is smaller by 3.76 mHa.

Next, a third layer was introduced by placing two additional basis atoms (six in total) in the same way as before: placing one directly above the 2nd atom within the second basis at ($\frac{2}{3}\frac{2}{3}\frac{2}{5}$) and the other at ($\frac{3}{3}\frac{3}{3}$ 0.462); vacuum convergence was ensured again by increasing $\boldsymbol{a_3}$ to $\boldsymbol{a_3}$=a_0(-$\frac{6}{3}\frac{6}{3}\frac{6}{3}$). An optimization of the atoms positions using the BFGS method finds an average intralayer bond length of $\boldsymbol{r_{intra}}$ = 5.33 Bohr with an average intralayer buckling angle of $\phi = 35.6°$. The algorithm also finds an average interlayer bond length of $\boldsymbol{r_{inter}}$ = 5.45 Bohr. Following this, the strain study found again that the HB phase remains more stable, but the difference in energy between phases shrank to 6.18 mHa (compared to 8.09 mHa for the bilayer and 11.85 mHa for the monolayer).

However, while the strain study for the trilayer configuration ran, a new, more stable structure appeared. A more careful study of this behavior found that there are in fact, *several* unique trilayer structures that are more stable than the one first introduced. A strain study was completed on these structures and is shown alongside the other layer configurations in Figure 5.2. The local minimum of this new "rogue" structure appears to behave as though there are two surface layers, with an intermediate layer in between near $a_{2D} \sim 8.2$ $Bohr$ and is shown in Fig. 5.2(c), Fig. 5.5(b), and Fig. 5.6(b). These surface layers arrange themselves in a low-buckled-like configuration with a much smaller buckling angle $\phi_{avg} = 4.33°$ and a buckling height of $\Delta z_{avg} = 2.91$ $Bohr$. The interior arranges itself in a metallic, high-buckled-like configuration with a buckling angle of $\phi = 40.92°$ and a buckling height of $\Delta z = 3.89$ $Bohr$. Unfortunately, this metallic behaviour destroys the QSH insulating phase and can no longer be considered topologically interesting. There are however, other *structural*

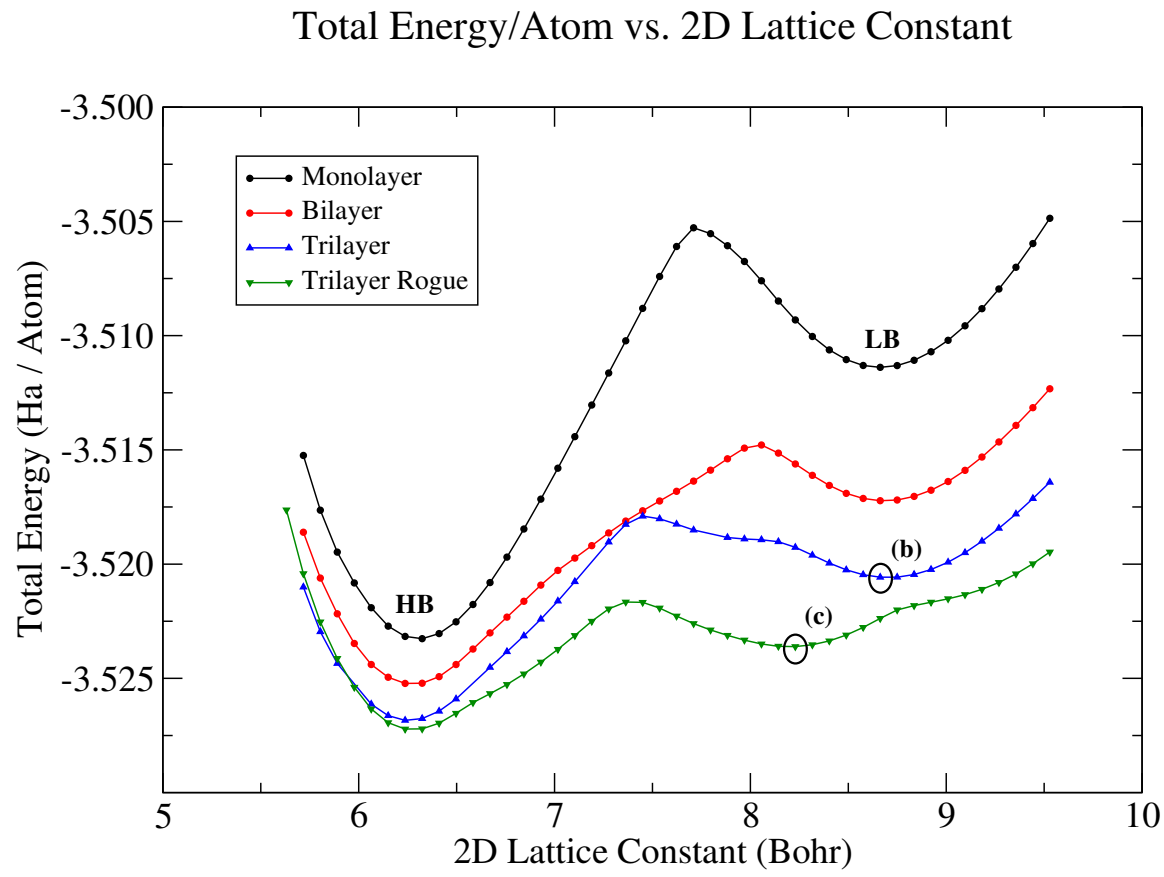

(a)

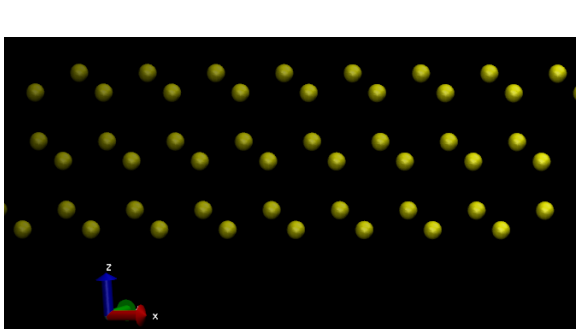

(b)

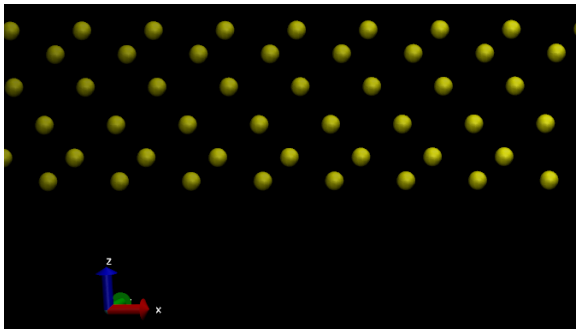

(c)

Figure 5.2: Plot of total energy against lattice constant demonstrating the stability of the HB and LB phases of stanene (a). Each layer configuration is shown with the addition of the rogue trilayer structure discovered while straining the trilayer configuration of stanene. Visualization of the local minima of the trilayer configuration (b) and the rogue trilayer configuration (c).

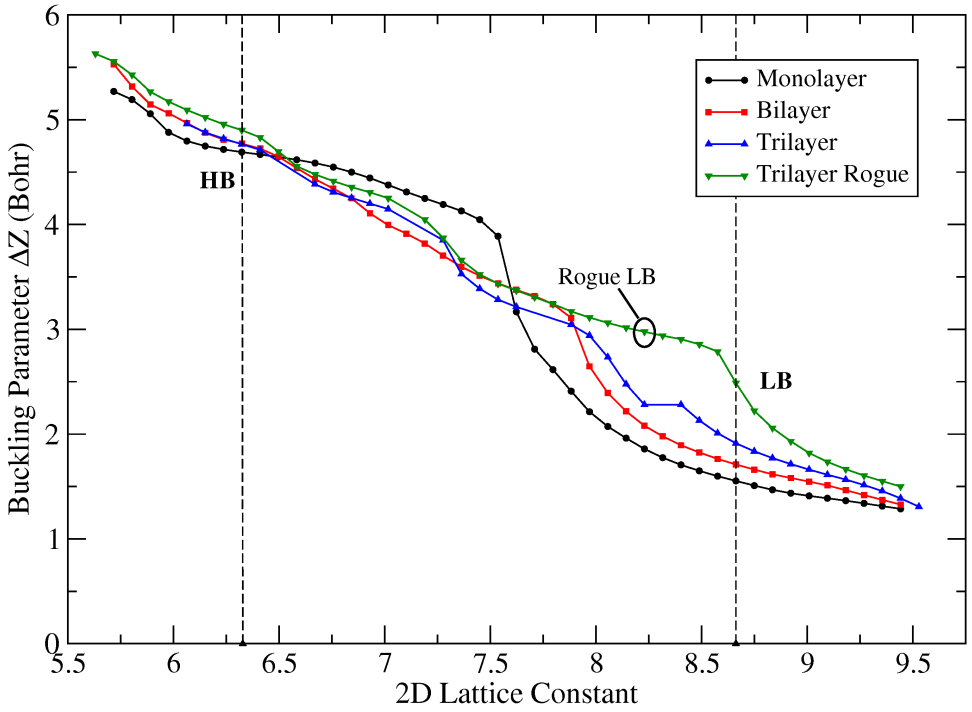

Figure 5.3: Plot of the buckling parameter Δz against lattice constant as each configuration is strained. The monolayer makes the most dramatic transition from the LB to the HB phase while the bilayer and trilayer make a slower transition into the HB phase. The trilayer rogue structure, however, actually flattens before buckling higher in the HB phase.

investigations that can be explored with this material as these configurations are unique to the bulk phases of tin.

Note also that the *Trilayer Rogue* curve in Figure 5.2 demonstrates that there are at least two other distinct structures (three in total) which can be identified by examining each parabola within this curve. At a_{2D} values larger than ~ 8.8 *Bohr* the BFGS optimization algorithm finds a new metastable configuration for the trilayer. This configuration is closer to a stacking of three low-buckled layers rather than the surface-interior layer configuration of the local minimum. This configuration possesses a surface layer buckling of $\Delta z = 1.223$ *Bohr*, a surface buckling angle of $\phi = 12.61°$, an interior buckling of $\Delta z = 3.034$ *Bohr*, and an interior buckling angle of $\phi = 33.32°$. Finally, the global minimum of these "rogue" structures begins to lose the distinct, buckled trilayer configuration and, while it still possesses different buckling heights between the surface and interior layers, the structure appears to

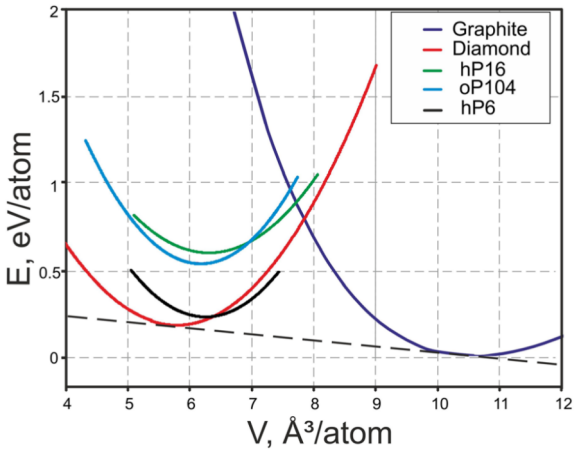

Figure 5.4: Plot of energy per atom against volume per atom for several allotropes of carbon demonstrating the competing structures of graphite (purple) and diamond (red) [7].

become six separate HCP-like layers. The first and last pair of layers have a buckling height of $\Delta z = 1.43$ *Bohr* and buckling angle $\phi = 13.37°$ while the interior pair of layers posses a buckling height of $\Delta z = 4.44$ *Bohr* and a buckling angle of $\phi = 45°$. Lastly, a transition between each of these three configurations is fairly smooth; which indicates that it does not require a significant amount of strain to induce when compared to the monolayer.

A similar phenomenom can be seen in the different allotropes of carbon in a plot of energy against volume (see Figure 5.4). At low volumes, the diamond configuration of carbon more stable, however, as volume is increased, the diamond configuration becomes less and less stable, and the graphite configuration begins to win out and becomes the more stable allotrope. Note the intersection of the two curves at ~ 7.9 $Å^3/atom$ indicating the transition between the stabler allotrope. The BFGS algorithm finds a similar behavior for the trilayer rogue structure near ~ 8.8 *Bohr* in Figure 5.2 which suggests that there are several allotropes of trilayer stanene that are metastable. The slope of the dashed line in Fig. 5.4 indicates the pressure required to induce a transition between the two allotropes and in fact, while transitioning between the two phases, the material will hybridize between diamond and graphite allotropes instead of remaining in either one or the other in order to minimize the total energy.

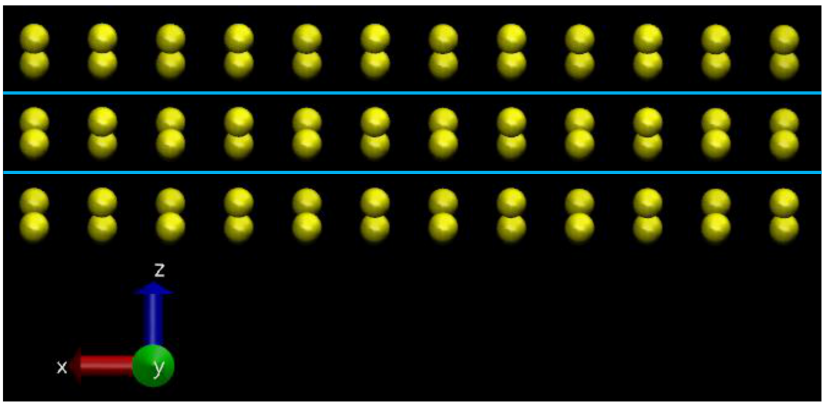

(a)

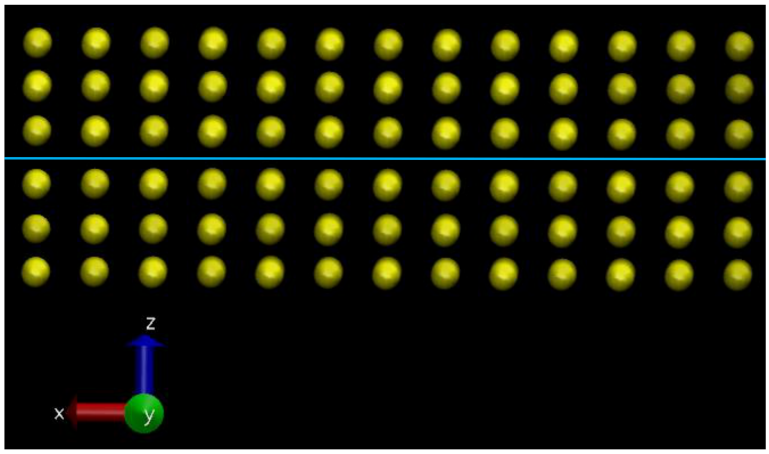

(b)

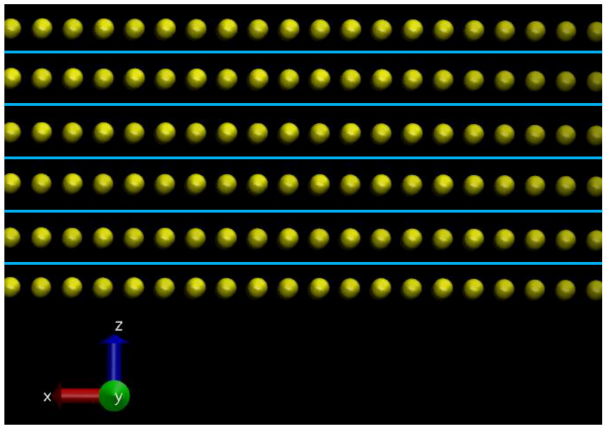

(c)

Figure 5.5: Visualization of the *Trilayer Rogue* structures for the: stacked trilayer (a), the surface-interior layer combination (b), and the stable HCP-like configuration (c).

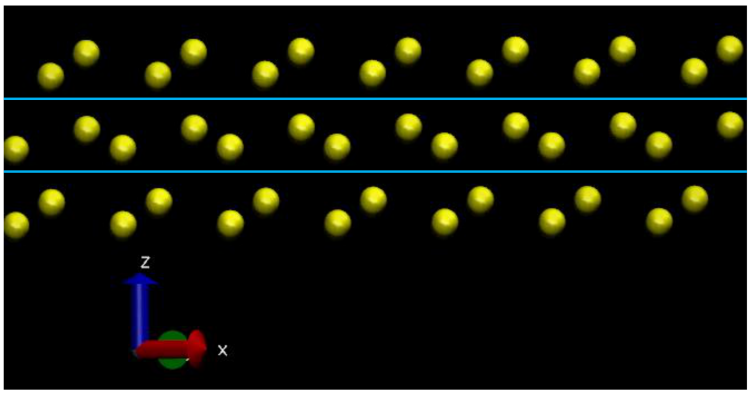

(a)

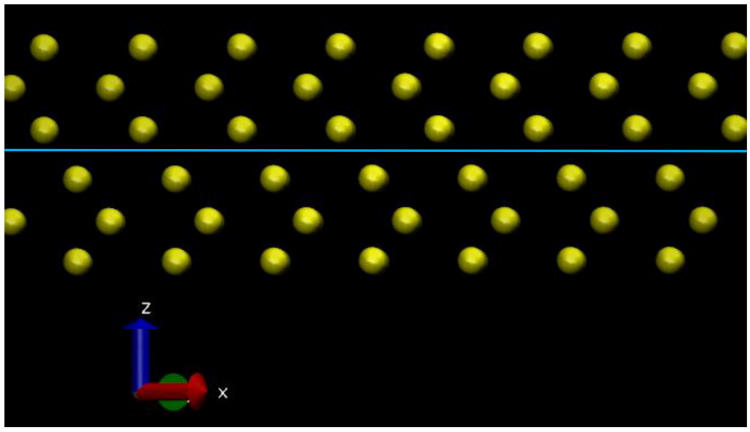

(b)

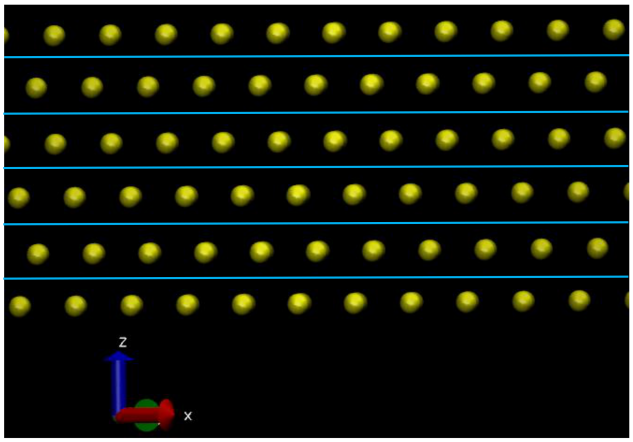

(c)

Figure 5.6: Visualization of the *Trilayer Rogue* structures for the: stacked trilayer (a), the surface-interior layer combination (b), and the stable HCP-like configuration (c).

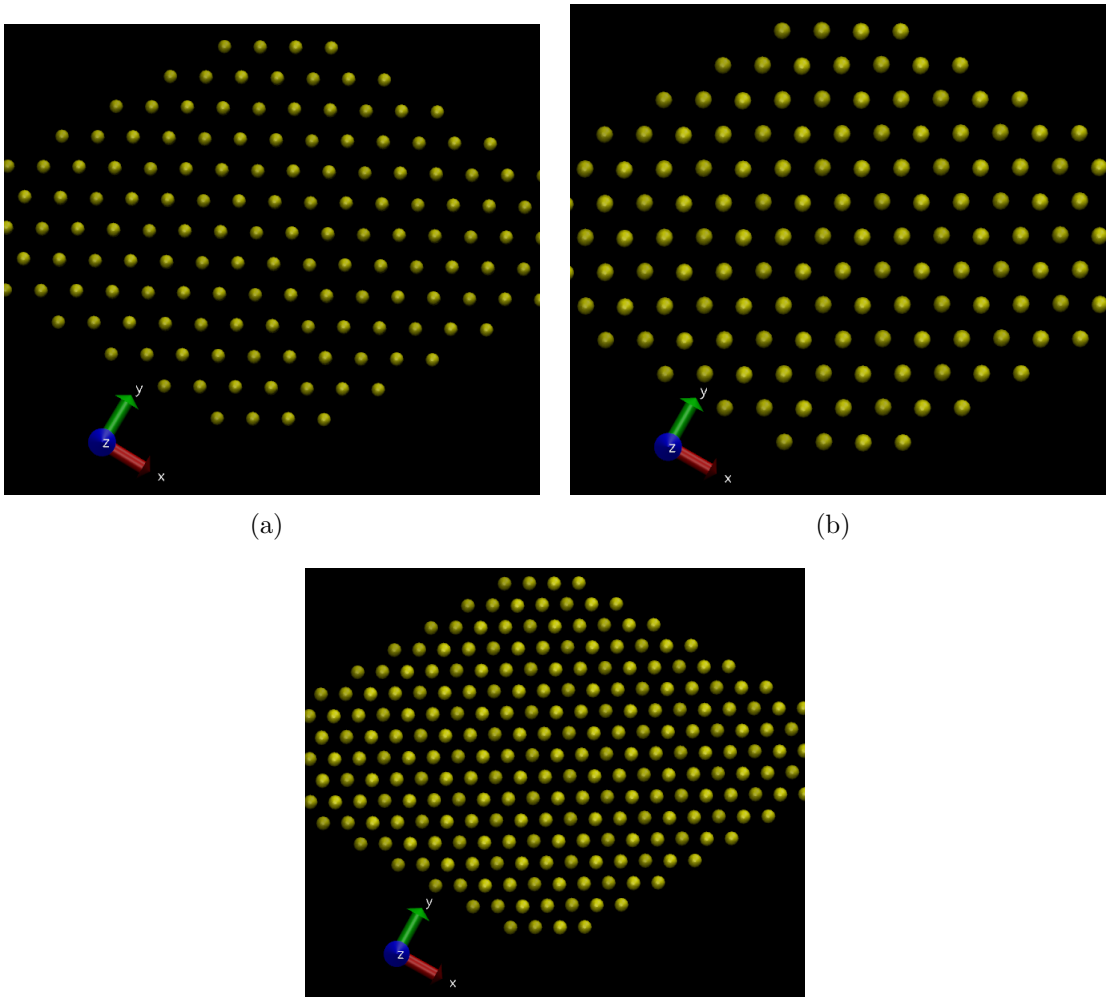

(a) (b)

(c)

Figure 5.7: Visualization of a top-down view of the *Trilayer Rogue* structures for the: stacked trilayer (a), the surface-interior layer combination (b), and the stable HCP-like configuration (c). Note that each of these configuration possesses hexagonal symmetry when viewed from this direction.

5.3 Electronic Structure of Multiple Layers

In addition to the structural studies of multiple layers, electronic structure was also explored. This was done primarily to conclude if the multilayer configurations remained to be semiconductors and thus still possess the characteristics of a QSH insulator. Only the LB phase's electronic structure for the trilayer and bilayer were calculated as the HB configurations were assumed to be metallic, like the monolayer, and the results of these calculations are found in Figure 5.8. A previous study [30] has shown that bilayer stanene is metallic, however, our results demonstrate that the bilayer configuration is semimetallic, i.e. the point at which the conduction band crosses the fermi level is not the same point at which the topmost valence band reaches the fermi level. The same can be said of the trilayer's electronic structure (Fig. 5.8). The reason for observing this semimetallic behavior (rather than metallic) is because these band structures utilize the Becke-Johnson correction which obtains more accurate eigenvalues. We demonstrate this by comparing the band structure of the bilayer using the PBEsol and BJ functionals (see Fig. 5.10).

In addition, the introduction of multiple layers introduces new subbands in the band structure. Many of these new bands are replications of states that are present in the monolayer, with a copy for each new layer of stanene. However, in the trilayer, an additional, apparently unrelated state appears at the top of the valence bands. The bandstructure of bilayer stanene in the LB configuration is semimetallic with a local band gap of 72.1 meV at the K point. Trilayer stanene is also semimetallic with a local gap of 220.7 meV at the K point.

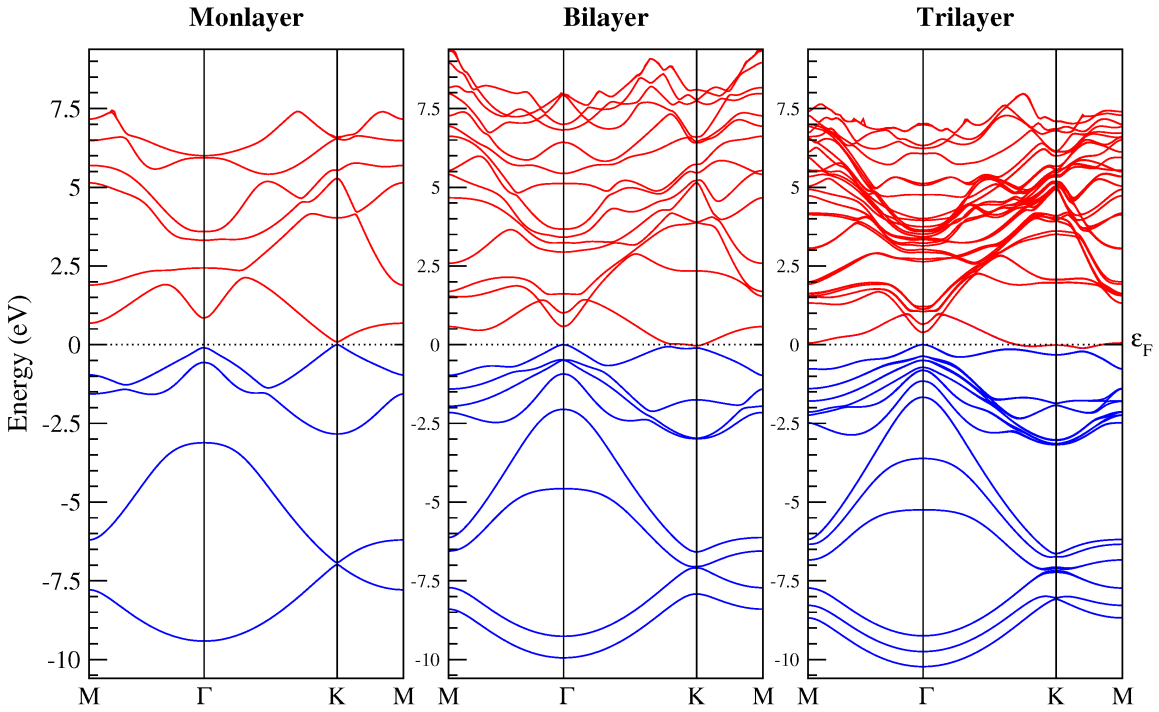

Figure 5.8: Band structure for the LB configuration of (left) monolayer stanene, (middle) bilayer stanene, (right) trilayer stanene. There is a gap at the K of 72.1 meV and 220.7 meV for the bilayer and trilayer respectively.

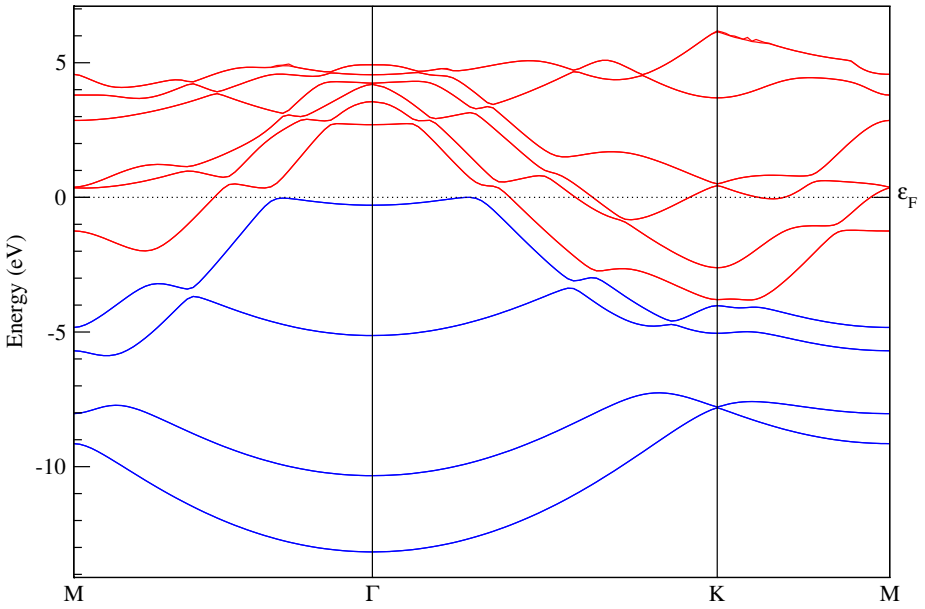

Figure 5.9: Band structure of the high-buckled phase of monolayer stanene. The penetration of the conduction bands below the fermi energy indicates that this configuration is metallic and thus can no longer support a QSH insulating state.

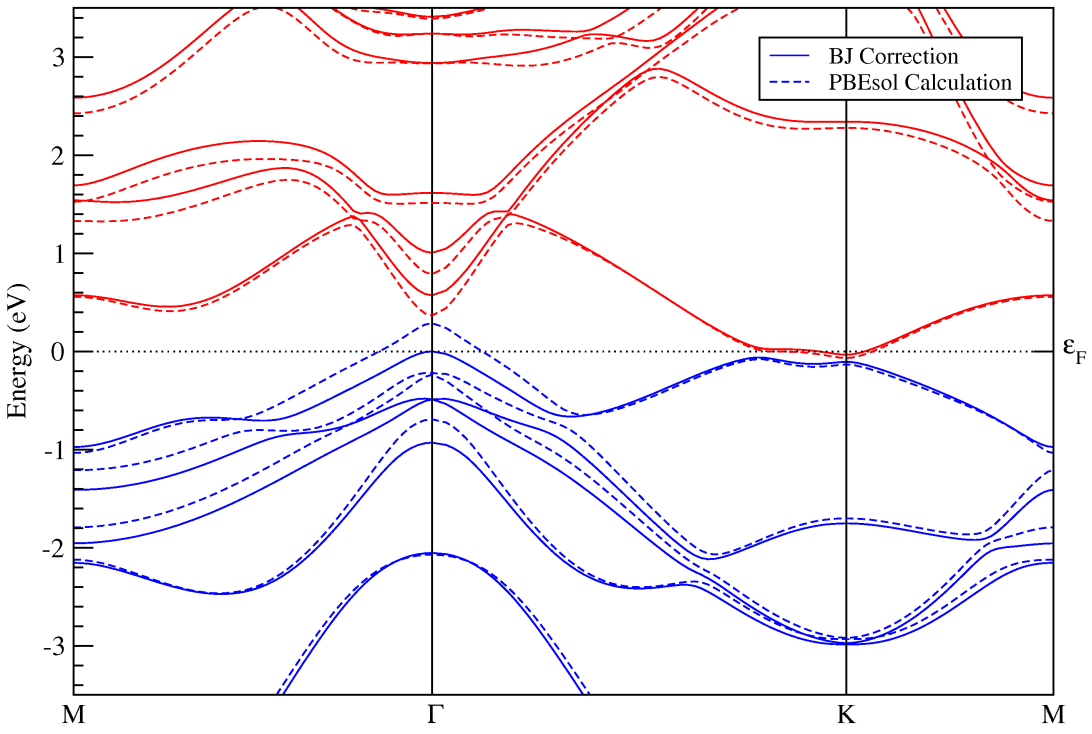

Figure 5.10: Bilayer bandstructure demonstrating the improvement in eigenvalues that the Becke-Johnson correction provides over the PBEsol functional.

Chapter 6

Conclusions

This chapter provides a summation and discussion of the research presented in this thesis. This includes a discussion of similarities in the electronic structure of stanene and graphene as well as a discussion of the merit of the BJ correction. Following this, the structural properties of multilayer stanene are summarized and discussed. The chapter then ends with a discussion of future work that can be explored in order to further stabilize and tune the electronic structure of stanene.

6.1 Discussion

In this thesis, the structural and electronic properties of monolayer and multilayer stanene was explored. To accomplish this, we used DFT with a plane-wave basis and pseudopotential approximation to model our system. This work attempted to accomplish the following goals: confirm monolayer stanene to be a QSH insulator, test the introduction of multiple layers of stanene as a method of stabilization, and to utilize the Becke-Johnson method within these systems in the hope of obtaining a more accurate band structure than typical PBE models.

The groundwork for this investigation was accomplished in chapter 3 through the comparison of our model's structural and electronic properties to experiment; which demonstrated that, for a bulk α-Sn system, the PBEsol functional finds lattice constants accurately

while the BJ functional finds more accurate eigenvalues. Additionally, we established that our consideration of spin-orbit coupling can break degeneracies within band structure calculations.

In Chapter 4 we were able to derive a structural description of monolayer stanene from its bulk counterpart, α-Sn. We constructed primitive translations vectors, initial basis atom positions and lattice constants. We then optimized this structure and found that, when monolayer stanene is isloated, the bond length, buckling angle, and lattice constant all decrease slightly.

In addition, we also calculated the electronic structure and density of states of monolayer stanene. We found that, when SOC is introduced, a band gap opens up at the K point which is indicative of a QSH insulating phase. In addition, we found the same linear dispersion of the HOMO and LUMO bands at the K point as that of graphene. These bands possess a fermionic-like behaviour and can be fit to find a "local" speed of light, known as the fermi velocity, as well as a spin-orbit coupling strength. These parameters can be used in tight binding models [15] which could be a useful platform for modeling charge transport in nanoribbons or perhaps as a type of topological field effect transistor, given stanene's ability to transition from a topological to trivial insulator when exposed to electric fields [68].

In Chapter 5, we did a structural study on monolayer stanene. In it, we compressed the lattice and confirmed that LB stanene is a metastable state and showed that the HCP-like HB phase is more stable. In order to alleviate this, we tried introducing a second and third layer of stanene and did the same strain study. It found that the HB phase remains the most stable state for all of these configurations. However, figure 5.2 suggests that further additions of layers *could* stabilize the LB phase, but it is unlikely that the QSH insulating phase would persist. Additionally, it was found that the trilayer unexpectedly prefers to arrange itself nanostructures unique to few layers of tin. These structures are novel and should be further explored.

Lastly, we calculated the electronic structure of these multi-layer configurations and

found that the LB-like phases are semimetallic. This conflicts with previous work [30] that has shown bilayer stanene to be metallic. This is directly caused by the use of the Becke-Johnson method for handling the exchange potential, rather than the traditional PBE or PBEsol.

6.2 Future Work

This study focused on primarily one method of stabilization, the introduction of multiple layers, of which there are many which can be explored. Anything that is able to saturate the dangling surface bonds of monolayer stanene, such as hydrogen or fluorine, could prove useful in ensuring stability. In addition, substrates may also prove fruitful in stabilization. Materials such as SrTe and PbTe have shown to preserve the QSH insulating phase while also tuning the band gap [27]. Hexagonal Boron Nitride (hBN) could also play a role in stabilization. The large band gap could preserve the topologically interesting aspects of stanene, while also saturating the surface bonds. Lastly, bilayer stanene requires further investigation as the repulsion of HOMO and LUMO bands near the K point is similar to that of bilayer graphene [69].

Additionally, methods for a phase transition between a topological and trivial insulator or metal should be explored. Bilayer stanene has already been shown that a transition between a topological insulator and normal metal can be induced through strain both in this thesis and in [30]. External electric fields have also been shown to induce a transition between a topological and trivial insulator in monolayer stanene [68]. A further investigation of a phase transition between topological and trivial insulator for bilayer stanene could also be explored.

Appendix A

List of Acronyms

ABINIT Open-source density functional theory coding package

APE Atomic Pseudopotential Engine

BFGS Broyden Fletcher Goldfarb Shanno

BJ Becke-Johnson

BZ Brillouin Zone

DFT Density Functional Theory

DOS Density of States

fcc face-centered cubic

GGA Generalized Gradient Approximation

m-GGA meta-Generalized Gradient Approximation

HB High-Buckled

HCP Hexagonal Close Packed

HE Hall Effect

HEG Homogeneous Electron Gas

HOMO Highest Occupied Molecular Orbital

KS Kohn-Sham

LB Low-Buckled

LUMO Lowest Unoccupied Molecular Orbital

OEP Opitmized Effective Potential

PBE Perdew-Burke-Ernzerhof

PBE Variant of PBE to improve calculations on solids

QH Quantum Hall

QHE Quantum Hall Effect

QSH Quantum Spin Hall

QSHE Quantum Spin Hall Effect

SCF Self-consistent field

SO Spin-Orbit

nSO non-Spin-Orbit

SOC Spin-Orbit Coupling

TKNN Topological invariant used to define a quantum Hall state

TI Topological Insualtor

TM Troulier Martins

TRIM Time Reversal Invariant Momentum

VMD Visual Molecular Dynamics software package

XC Exchange Correlation

Bibliography

[1] Ashok K. Sood, Isaac Lund, Yash R. Puri, Harry Efstathiadis, Pradeep Haldar, Nibir K. Dhar, Jay Lewis, Madan Dubey, Eugene Zakar, Priyalal Wijewarnasuriya, Dennis L. Polla, and Michael Fritze. *Review of graphene technology and its applications for electronic devices*. In Farzad Ebrahimi, editor, "Graphene - New Trends and Developments," chapter 03. InTech, Rijeka (2015). doi:10.5772/61316. URL `http://dx.doi.org/10.5772/61316`.

[2] Feng-feng Zhu, Wei-jiong Chen, Yong Xu, Chun-lei Gao, Dan-dan Guan, Can-hua Liu, Dong Qian, Shou-Cheng Zhang, and Jin-feng Jia. *Epitaxial growth of two-dimensional stanene*. Nature Materials **14**, 1020 (2015). doi:10.1038/nmat4384.

[3] Richard Martin. *Electronic Structure: Basic Theory and Methods*. Cambridge University Press (2004).

[4] T. Brudevoll, D. S. Citrin, M. Cardona, and N. E. Christensen. *Electronic structure of α- sn and its dependence on hydrostatic strain*. Phys. Rev. B **48**, 8629 (Sep 1993). doi: 10.1103/PhysRevB.48.8629. URL `http://link.aps.org/doi/10.1103/PhysRevB.48.8629`.

[5] Charles Kittel. *Introduction to Solid State Physics*. John Wiley & Sons (2005).

[6] William Humphrey, Andrew Dalke, and Klaus Schulten. *VMD – Visual Molecular Dynamics*. Journal of Molecular Graphics **14**, 33 (1996).

[7] Yulia A. Kvashnina, Alexander G. Kvashnin, and Pavel B. Sorokin. *Investigation of new superhard carbon allotropes with promising electronic properties*. Journal of Applied Physics **114(18)**, 183708 (2013). doi:10.1063/1.4829002. URL `http://dx.doi.org/10.1063/1.4829002`.

[8] Pulickel Ajayan, Philip Kim, and Kaustav Banerjee. *Two-dimensional van der waals materials*. Physics Today **69**, 38. doi:10.1063/PT.3.3297.

[9] Deep Jariwala, Vinod K. Sangwan, Lincoln J. Lauhon, Tobin J. Marks, and Mark C. Hersam. *Emerging device applications for semiconducting two-dimensional transition metal dichalcogenides*. ACS Nano **8(2)**, 1102 (2014). doi:10.1021/nn500064s. PMID: 24476095, URL `http://dx.doi.org/10.1021/nn500064s`.

[10] Srinivasa Reddy Tamalampudi, Yi-Ying Lu, Rajesh Kumar U., Raman Sankar, Chun-Da Liao, Karukanara Moorthy B., Che-Hsuan Cheng, Fang Cheng Chou, and Yit-Tsong Chen. *High performance and bendable few-layered inse photodetectors with broad spectral response*. Nano Letters **14(5)**, 2800 (2014). doi:10.1021/nl500817g. PMID: 24742243, URL `http://dx.doi.org/10.1021/nl500817g`.

[11] Akhtar Meysam, George Anderson, Rong Zhao, Adel Alruqi, Joanna E. Mroczkowska, Gamini Sumanasekera, and Jacek B. Jasinski. *Recent advances in synthesis, properties, and applications of phosphorene*. nppj @D Materials and Applications **1(5)** (2017). doi: 10.1038/s41699-017-0007-5. URL `http://dx.doi.org/10.1038/s41699-017-0007-5`.

[12] Changgu Lee, Xiaoding Wei, Jeffrey W. Kysar, and James Hone. *Measurement of the elastic properties and intrinsic strength of monolayer graphene*. Science **321(5887)**, 385 (2008). doi:10.1126/science.1157996.

[13] Alexander A. Balandin, Suchismita Ghosh, Wenzhong Bao, Irene Calizo, Desalegne Teweldebrhan, Feng Miao, and Chun Ning Lau. *Superior thermal conductivity of single-layer graphene*. Nano Letters **8(3)**, 902 (2008). doi:10.1021/nl0731872. URL `http://dx.doi.org/10.1021/nl0731872`.

[14] J. Scott Bunch, Scott S. Verbridge, Jonathan S. Alden, Arend M. van der Zande, Jeevak M. Parpia, Harold G. Craighead, and Paul L. McEuen. *Impermeable atomic membranes from graphene sheets*. Nano Letters **8(8)**, 2458 (2008). doi:10.1021/nl801457b. URL `http://dx.doi.org/10.1021/nl801457b`.

[15] A. H. Castro Neto, F. Guinea, N. M. R. Peres, K. S. Novoselov, and A. K. Geim. *The electronic properties of graphene*. Rev. Mod. Phys. **81**, 109 (Jan 2009). doi:10.1103/RevModPhys.81.109. URL `https://link.aps.org/doi/10.1103/RevModPhys.81.109`.

[16] Max C. Lemme. *Current status of graphene transistors*. Solid State Phenomena **156-158**, 499 (2010). doi:10.4028/www.scientific.net/SSP.156-158.499.

[17] C. B. McKitterick, D. E. Prober, H. Vora, and X. Du. *Ultrasensitive graphene far-infrared power detectors*. Journal of Physics: Condensed Matter **27(16)** (APR 29 2015). doi:10.1088/0953-8984/27/16/164203.

[18] Xiaosong Wu, Mike Sprinkle, Xuebin Li, Fan Ming, Claire Berger, and Walt A. de Heer. *Epitaxial-graphene/graphene-oxide junction: An essential step towards epitaxial graphene electronics*. Phys. Rev. Lett. **101**, 026801 (Jul 2008). doi:10.1103/PhysRevLett.101.026801. URL `https://link.aps.org/doi/10.1103/PhysRevLett.101.026801`.

[19] Brian Standley, Wenzhong Bao, Hang Zhang, Jehoshua Bruck, Chun Ning Lau, and Marc Bockrath. *Graphene-based atomic-scale switches*. Nano Letters **8(10)**, 3345 (2008). doi:10.1021/nl801774a. URL `http://dx.doi.org/10.1021/nl801774a`.

[20] T. J. Echtermeyer, M. C. Lemme, M. Baus, B. N. Szafranek, A. K. Geim, and H. Kurz. *Nonvolatile switching in graphene field-effect devices*. IEEE Electron Device Letters **29(8)**, 952 (Aug 2008). doi:10.1109/LED.2008.2001179.

[21] Yi Zheng, Guang-Xin Ni, Chee-Tat Toh, Ming-Gang Zeng, Shu-Ting Chen, Kui Yao, and Barbaros zyilmaz. *Gate-controlled nonvolatile graphene-ferroelectric memory*. Applied Physics Letters **94(16)**, 163505 (2009). doi:10.1063/1.3119215. URL `http://dx.doi.org/10.1063/1.3119215`.

[22] Dmytro Pesin and Allan H. MacDonald. *Spintronics and pseudospintronics in grpahene and topological insulators*. Nature Materials **11**, 409 (2012). doi:doi:10.1038/nmat3305. URL `http://www.nature.com/nmat/journal/v11/n5/full/nmat3305.html`.

[23] N. D. Drummond, V. Zólyomi, and V. I. Fal'ko. *Electrically tunable band gap in silicene*. Phys. Rev. B **85**, 075423 (Feb 2012). doi:10.1103/PhysRevB.85.075423. URL `https://link.aps.org/doi/10.1103/PhysRevB.85.075423`.

[24] Cheng-Cheng Liu, Wanxiang Feng, and Yugui Yao. *Quantum spin hall effect in silicene and two-dimensional germanium*. Phys. Rev. Lett. **107**, 076802 (Aug 2011). doi:10.1103/PhysRevLett.107.076802. URL `https://link.aps.org/doi/10.1103/PhysRevLett.107.076802`.

[25] Yong Xu, Binghai Yan, Hai-Jun Zhang, Jing Wang, Gang Xu, Peizhe Tang, Wenhui Duan, and Shou-Cheng Zhang. *Large-gap quantum spin hall insulators in tin films*. Phys. Rev. Lett. **111**, 136804 (Sep 2013). doi:10.1103/PhysRevLett.111.136804. URL `https://link.aps.org/doi/10.1103/PhysRevLett.111.136804`.

[26] Sumit Saxena, Raghvendra Pratap Chaudhary, and Shobha Shukla. *Stanene: Atomically thick free-standing layer of 2d hexagonal tin*. Nature Scientific Reports **6(31073)** (2016). doi:10.1038/srep31073.

[27] Yong Xu, Peizhe Tang, and Shou-Cheng Zhang. *Large-gap quantum spin hall states in decorated stanene grown on a substrate*. Phys. Rev. B **92**, 081112 (2015). doi:10.1103/PhysRevB.92.081112.

[28] William G. Vandenberghe. *Imperfect two-dimensional topological insulator field-effect transistors*. Nature Communications **8(14184)** (2017). doi:10.1038/ncomms14184.

[29] P. Rivero J. Yan V. Garcia-Suarez J .Ferrer S. Barraza-Lopez. *Stability and poperties of high-buckled two-dimensional tin and lead*. Physical Review B **90** (Dec 2014). ISSN 1098-0121. doi:10.1103/PhysRevB.90.241408.

[30] Chengxi Huang, Jian Zhou, Haiping Wu, Kaiming Deng, Puru Jena, and Erjun Kan. *Quantum phase transition in germanene and stanene bilayer: From normal metal to topological insulator*. The Journal of Physical Chemistry Letters **7(10)**, 1919 (2016). doi:10.1021/acs.jpclett.6b00651. URL `http://dx.doi.org/10.1021/acs.jpclett.6b00651`.

[31] R. J. Elliott. *Theory of the effect of spin-orbit coupling on magnetic resonance in some semiconductors*. Phys. Rev. **96**, 266 (1954). doi:10.1103/PhysRev.96.266. URL https://link.aps.org/doi/10.1103/PhysRev.96.266.

[32] R. J. Elliot. *Spin-orbit coupling in band theory–caharacter tables for some "double" space groups* pages 280–287 (1954).

[33] M. Born and R. Oppenheimer. *Zur quantentheorie der molekeln*. Annalen der Physik **389(20)**, 457 (1927). doi:10.1002/andp.19273892002.

[34] P. Hohenberg and W. Kohn. *Inhomogeneous electron gas*. Phys. Rev. **136**, B864 (Nov 1964). doi:10.1103/PhysRev.136.B864. URL https://link.aps.org/doi/10.1103/PhysRev.136.B864.

[35] W. Kohn and L. J. Sham. *Self-consistent equations including exchange and correlation effects*. Phys. Rev. **140**, A1133 (Nov 1965). doi:10.1103/PhysRev.140.A1133. URL https://link.aps.org/doi/10.1103/PhysRev.140.A1133.

[36] Jesse Watson. *Testing the Tran-Blaha Approach for Band gap Calculations in a Pseudo-Potential Environment*. Master's thesis, Ball State University (December 2013).

[37] Aurora Pribram-Jones, David A. Gross, and Kieron Burke. *Dft: A theory full of holes?* Anual Review of Physical Chemistry **66**, 283 (2015). doi:10.1146/annurev-physchem-040214-121420.

[38] John P. Perdew, Kieron Burke, and Matthias Ernzerhof. *Generalized gradient approximation made simple*. Phys. Rev. Lett. **77**, 3865 (1996). doi:10.1103/PhysRevLett.77.3865. URL https://link.aps.org/doi/10.1103/PhysRevLett.77.3865.

[39] John P. Perdew, Adrienn Ruzsinszky, Gábor I. Csonka, Oleg A. Vydrov, Gustavo E. Scuseria, Lucian A. Constantin, Xiaolan Zhou, and Kieron Burke. *Restoring the density-gradient expansion for exchange in solids and surfaces*. Phys. Rev. Lett. **100**, 136406 (2008).

[40] Axel D. Becke and Erin R. Johnson. *A simple effective potential for exchange*. The Journal of Chemical Physics **124(22)**, 221101 (2006). doi:10.1063/1.2213970. URL http://dx.doi.org/10.1063/1.2213970.

[41] R. T. Sharp and G. K. Horton. *A variational approach to the unipotential many-electron problem*. Phys. Rev. **90**, 317 (1953). doi:10.1103/PhysRev.90.317. URL https://link.aps.org/doi/10.1103/PhysRev.90.317.

[42] James D. Talman and William F. Shadwick. *Optimized effective atomic central potential*. Phys. Rev. A **14**, 36 (1976). doi:10.1103/PhysRevA.14.36. URL https://link.aps.org/doi/10.1103/PhysRevA.14.36.

[43] J. C. Slater. *A simplification of the hartree-fock method*. Phys. Rev. **81**, 385 (1951). doi:10.1103/PhysRev.81.385. URL https://link.aps.org/doi/10.1103/PhysRev.81.385.

[44] U. von Barth and C. D. Gelatt. *Validity of the frozen-core approximation and pseudopotential theory for cohesive energy calculations*. Phys. Rev. B **21**, 2222 (1980). doi: 10.1103/PhysRevB.21.2222. URL https://link.aps.org/doi/10.1103/PhysRevB.21.2222.

[45] Zach Nault. *Measureing the Quality of Generalized Gradient Approximations in a Density Function Theory Pseudopotential Environment for Solids*. Master's thesis, Ball State University (June 2013).

[46] E. H. Hall. *On a new action of the magnet on electric currents*. American Journal of Mathematics **2**, 287 (1879). ISSN 00029327, 10806377. URL http://www.jstor.org/stable/2369245.

[47] A. J. Turberfield, S. R. Haynes, P. A. Wright, R. A. Ford, R. G. Clark, J. F. Ryan, J. J. Harris, and C. T. Foxon. *Optical detection of the integer and fractional quantum hall effects in gaas*. Phys. Rev. Lett. **65**, 637 (Jul 1990). doi:10.1103/PhysRevLett.65.637. URL https://link.aps.org/doi/10.1103/PhysRevLett.65.637.

[48] Tsuneya Ando, Yukio Matsumoto, and Yasutada Uemura. *Theory of hall effect in a two-dimensional electron system*. Journal of the Physical Society of Japan **39(2)**, 279 (1975). doi:10.1143/JPSJ.39.279. URL http://dx.doi.org/10.1143/JPSJ.39.279.

[49] K. v. Klitzing, G. Dorda, and M. Pepper. *New method for high-accuracy determination of the fine-structure constant based on quantized hall resistance*. Phys. Rev. Lett. **45**, 494 (Aug 1980). doi:10.1103/PhysRevLett.45.494. URL https://link.aps.org/doi/10.1103/PhysRevLett.45.494.

[50] R. B. Laughlin. *Quantized hall conductivity in two dimensions*. Phys. Rev. B **23**, 5632 (May 1981). doi:10.1103/PhysRevB.23.5632. URL https://link.aps.org/doi/10.1103/PhysRevB.23.5632.

[51] Klaus von Klizing. *Developments in the quantum hall effect*. Phil. Trans. R. Soc. A **363**, 2203 (2005). doi:10.1098/rsta.2005.1640.

[52] Joseph Maciejko, Taylor L. Hughes, and Shou-Cheng Zhang. *The quantum spin hall effect*. Annual Review of Condensed Matter Physics **2**, 31 (2011). doi:10.1146/annurev-conmatphys-062910-140538.

[53] A. Bansil, Hsin Lin, and Tanmoy Das. *Colloquium : Topological band theory*. Rev. Mod. Phys. **88**, 021004 (Jun 2016). doi:10.1103/RevModPhys.88.021004. URL http://link.aps.org/doi/10.1103/RevModPhys.88.021004.

[54] M. Z. Hasan and C. L. Kane. *Colloquium : Topological insulators*. Rev. Mod. Phys. **82**, 3045 (Nov 2010). doi:10.1103/RevModPhys.82.3045. URL http://link.aps.org/doi/10.1103/RevModPhys.82.3045.

[55] Ziao-Liang Qi and Shou-Chen Zhang. *Topological insulators and superconductors*. Reviews of Modern Physics **83**, 1057. doi:10.1103\RevModPhys.83.1057.

[56] Marcel Franz and Molenkamp Laurens. Elsevier (2013).

[57] X. Gonze, B. Amadon, P.-M. Anglade, J.-M. Beuken, F. Bottin, P. Boulanger, F. Bruneval, D. Caliste, R. Caracas, M. Ct;, T. Deutsch, L. Genovese, Ph. Ghosez, M. Giantomassi, S. Goedecker, D.R. Hamann, P. Hermet, F. Jollet, G. Jomard, S. Leroux, M. Mancini, S. Mazevet, M.J.T. Oliveira, G. Onida, Y. Pouillon, T. Rangel, G.-M. Rignanese, D. Sangalli, R. Shaltaf, M. Torrent, M.J. Verstraete, G. Zerah, and J.W. Zwanziger. *Abinit: First-principles approach to material and nanosystem properties.* Computer Physics Communications **180(12)** (2009). doi:10.1016/j.cpc.2009.07.007. URL `http://www.sciencedirect.com/science/article/pii/S0010465509002276`.

[58] X Gonze, G Rignanese, M Verstraete, J Betiken, Y Pouillon, R Caracas, F Jollet, M Torrent, G Zerah, M Mikami, P Ghosez, M Veithen, J-Y Raty, V Olevano, F Bruneval, L Reining, R Godby, G Onida, D Hamann, and D Allan. *A brief introduction to the abinit software package.* Zeitschrift für Kristallographie.(Special issue on Computational Crystallography.) **220**, 558 (2005).

[59] M. Oliveira and F. Nogueira. *Atomic Pseudopotential Engine* (2012). URL `http://www.tddft.org/programs/APE/node/9`.

[60] N. Troullier and José Luís Martins. *Efficient pseudopotentials for plane-wave calculations.* Phys. Rev. B **43**, 1993 (Jan 1991). doi:10.1103/PhysRevB.43.1993. URL `https://link.aps.org/doi/10.1103/PhysRevB.43.1993`.

[61] Hong Jiang. *Band gaps from the tran-blaha modified becke-johnson approach: A systematic investigation.* The Journal of Chemical Physics **138(13)**, 134115 (2013). doi:10.1063/1.4798706. URL `http://dx.doi.org/10.1063/1.4798706`.

[62] Hendrik J. Monkhorst and James D. Pack. *Special points for brillouin-zone integrations.* Phys. Rev. B **13**, 5188 (Jun 1976). doi:10.1103/PhysRevB.13.5188. URL `https://link.aps.org/doi/10.1103/PhysRevB.13.5188`.

[63] H. Bernhard Schlegel. *Optimization of equilibrium geometries and transition structures.* Journal of Computational Chemistry **3(2)**, 214 (1982). ISSN 1096-987X. doi:10.1002/jcc.540030212. URL `http://dx.doi.org/10.1002/jcc.540030212`.

[64] Cheng-Cheng Liu, Wanxiang Feng, and Yugui Yao. *Quantum spin hall effect in silicene and two-dimensional germanium.* Phys. Rev. Lett. **107**, 076802 (Aug 2011). doi:10.1103/PhysRevLett.107.076802.

[65] Dmytro Pesin and Allan H. MacDonald. *Spintronics and pseudospintronics in graphene and topological insulators.* Nature Materials **11(5)**, 409 (2012).

[66] J. L. McChesney, Aaron Bostwick, Taisuke Ohta, Thomas Seyller, Karsten Horn, J. González, and Eli Rotenberg. *Extended van hove singularity and superconducting instability in doped graphene.* Phys. Rev. Lett. **104**, 136803 (Apr 2010). doi:10.1103/PhysRevLett.104.136803. URL `https://link.aps.org/doi/10.1103/PhysRevLett.104.136803`.

[67] I. Brihuega, P. Mallet, H. González-Herrero, G. Trambly de Laissardière, M. M. Ugeda, L. Magaud, J. M. Gómez-Rodríguez, F. Ynduráin, and J.-Y. Veuillen. *Unraveling the intrinsic and robust nature of van hove singularities in twisted bilayer graphene by scanning tunneling microscopy and theoretical analysis*. Phys. Rev. Lett. **109**, 196802 (2012). doi:10.1103/PhysRevLett.109.196802. URL `https://link.aps.org/doi/10.1103/PhysRevLett.109.196802`.

[68] Bas Houssa, Micheland van den Broek, Konstantina Iordanidou, Anh Khoa Augustin Lu, Geoffrey Pourtois, Jean-Pierre Locquet, Valery Afanas'ev, and André Stesmans. *Topological to trivial insulating phase transition in stanene*. Nano Research **9(3)**, 774 (2016). doi:10.1007/s12274-015-0956-y. URL `http://dx.doi.org/10.1007/s12274-015-0956-y`.

[69] Edward McCann. *Asymmetry gap in the electronic band structure of bilayer graphene*. Phys. Rev. B **74**, 161403 (Oct 2006). doi:10.1103/PhysRevB.74.161403. URL `https://link.aps.org/doi/10.1103/PhysRevB.74.161403`.